



Cite this: *J. Mater. Chem. C*,
2024, 12, 10775

Strategies for suppressing dark current of perovskite photodiodes towards reliable optoelectronic applications

Yue Wang, *^a Qing Song, ^a Deli Li, *^a Yang Liu, ^a Yang Wang ^a and Yonghua Chen *^b

Photodetection is crucial for advancements in next-generation technologies, including Internet of Things, intelligent perception, augmented and virtual reality, and human-machine interactions. Metal halide perovskites (MHPs) show unique properties that allow for the creation of straightforward diode structures, enabling efficient photogeneration and charge collection across a broad spectrum of wavelengths, from ionizing radiation to near-infrared. However, the presence of dark current (I_d) poses a significant challenge, affecting the performance of these devices. This review commences by outlining the essential performance measures impacted either directly or indirectly by I_d . Subsequently, it investigates the adjustable MHP materials employed in photodiodes, with a focus on their structural and morphological characteristics. We then explore the origins of I_d and highlight the crucial factors that impact the performance of MHP-based photodiodes (MHPPDs). Additionally, we examine various strategies to mitigate I_d , thereby improving device efficacy. Finally, we provide insights into future directions for reducing I_d in MHPPDs, potentially leading to further enhancements in photodetection technologies.

Received 29th March 2024,
Accepted 6th July 2024

DOI: 10.1039/d4tc01273a

rsc.li/materials-c

^a Strait Institute of Flexible Electronics (SIFE, Future Technologies), Fujian Key Laboratory of Flexible Electronics, Fujian Normal University and Strait Laboratory of Flexible Electronics (SLoFE), Fuzhou, 350117, China.

E-mail: ifeywang@fjnu.edu.cn, ifedlli@fjnu.edu.cn

^b Key Laboratory of Flexible Electronics (KLOFE) & Institute of Advanced Materials (IAM), Jiangsu National Synergistic Innovation Center for Advanced Materials (SICAM), Nanjing Tech University (NanjingTech), 30 South Puzhu Road, Nanjing 211816, Jiangsu, China. E-mail: iamyhchen@njtech.edu.cn



Yue Wang

Yue Wang completed his BSc in Applied Physics from Tiangong University in 2012 and his PhD in Optical Engineering from Beijing Jiaotong University in 2018. He then worked as a postdoctoral fellow focusing on organic and perovskite-based photodetectors at the MIIT Key Laboratory of Flexible Electronics, Northwestern Polytechnical University until 2020. Currently, he is an associate professor at the Strait

Laboratory of Flexible Electronics (SLoFE) and Fujian Normal University, specializing in perovskite optoelectronics and flexible electronics applications.

1. Introduction

Photodetection is crucial in diverse fields, including medical X-ray imaging, visible light capture, near-infrared medical imaging, short-wave infrared surveillance, and machine vision.^{1,2} These applications fundamentally depend on semiconductor photodetectors to transduce photons into electrical signals for processing, image reconstruction, and storage. Commonly, photodiodes and phototransistors constructed from inorganic semiconductors of silicon or III-V compounds, when integrated with thin-film transistors (TFTs) or complementary metal oxide semiconductors (CMOS) within a backplane architecture, enable the creation of intricate image sensor arrays suitable for modern optoelectronics.^{3,4}

The escalating demands of Internet of Things, intelligent perception, augmented and virtual reality, and human-machine interactions necessitate components that are lightweight, energy-efficient, miniature, and mechanically flexible.⁵ In response, researchers are exploring diverse semiconductor-based photodetectors,^{6,7} including organic materials, inorganic nanocrystals (NCs), quantum dots (QDs), and metal-halide perovskites (MHPs). MHPs, in particular, have attracted substantial attention due to their remarkable capabilities. These materials offer an ultra-broad spectral photodetection range, from ionizing radiation to near-infrared, achievable through

tailored adjustments in their organic and inorganic compositions. MHPs are not only derived from abundant resources and require low deposition temperatures but also form efficient single layers owing to their low exciton binding energy.⁸ When integrated into optoelectronic systems, they substantively augment functionality and precision in various sensing applications, such as photoplethysmography (PPG) sensors and pulse oximeters, enabling real-time and non-invasive monitoring.

While MHP-based photoconductors and phototransistors are notable for their impressive responsivity, facilitating signal amplification across applications, they tend to have slower response times and usually require additional biasing circuits for optimal performance. These factors demand careful consideration, particularly in the context of specific applications. Despite these challenges, the intrinsic properties of MHPs support the creation of simplified diode architectures that promote efficient photogeneration and charge collection with minimal losses. MHPPDs, employing configurations such as P-N, P-I-N, or Schottky junctions, can function without an external power supply. Applying an additional reverse bias can further enhance the efficiency of photogenerated carrier collection.⁹ Moreover, the progress in MHP-based devices benefits extensively from ongoing research on perovskite photovoltaics. Consequently, significant research efforts are directed at advancing our understanding of materials, device architectures, physical mechanisms, and processing techniques in this field. This endeavor seeks to improve the figures of merits (FOMs) of MHPPDs to bring them on par with those of their counterparts.

A critical parameter affecting MHPPDs' FOMs directly or indirectly, including the on-off ratio (OOR), linear dynamic range (LDR), specific detectivity (D^*), is the dark current (I_d). In MHPPDs, as illustrated in Fig. 1, carriers in an MHP film tend to drift towards their respective electrodes in the absence of a bias voltage. This behavior, facilitated by the unique properties

of MHPs, leads to complete depletion even without an applied bias voltage, significantly impacting the device's performance. The OOR is defined as the ratio of the photocurrent generated when the photodiode is exposed to light (on-state) to I_d when it is not exposed to light (off-state). This ratio indicates how effectively a photodiode can distinguish between the presence and absence of light signals. Therefore, reducing I_d in MHPPDs while preserving the photocurrent can considerably enhance the OOR. The LDR represents a valuable feature for MHPPDs where the output, such as photocurrent or responsivity, remains stable across a broad spectrum of incident light intensities. Beyond this dynamic range, the light signals cannot be accurately detected due to the elevated levels of I_d .¹⁰ Additionally, the noise equivalent power (NEP) defines the minimum optical power a photodiode can differentiate from the noise current, indicating the sensitivity of the photodiode to weak light signals. Noise current (i_n) in units of $\text{A Hz}^{-1/2}$ primarily includes shot noise, thermal noise, and flicker noise, among which shot noise, arising from the discrete passage of electrons and holes, generally dominates. Thermal noise is linked to the random motion of charge carriers, and flicker noise can result from fluctuations in conductivity due to variations in the electron concentration.¹¹ Additionally, the influence of I_d in the practical industrial applications of photodiodes is substantial. For example, high I_d can rapidly reach the breakdown voltage of TFTs or CMOS, widely employed in imaging and sensing technology, rendering them ineffective.¹²

Furthermore, the I_d of MHPPDs plays a crucial role in direct radiation detection, specifically in X-ray imaging and ionizing radiation detection applications, enabling nondestructive inspection in medical, security, and scientific fields. In direct radiation X-ray detection, MHPPDs employ active layers with thicknesses up to millimeters to effectively block high-energy radiation photons, which raises the issue of less charge

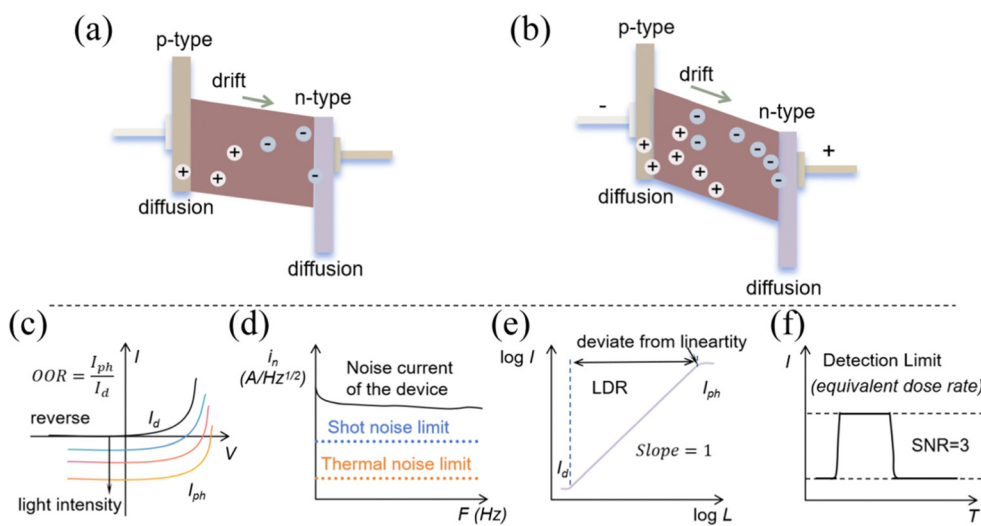


Fig. 1 Schematic illustration of the energy diagram of P-I-N photodiodes without bias (a) and under bias conditions (b). Schematic of the parameters influenced by I_d in photodiodes for light sensing and direct X-ray detection. (c) On-off ratio (OOR). (d) Noise current (i_n). (e) Linear dynamic range (LDR). (f) Detection limit.

collection efficiency for the devices. One effective solution to overcome this challenge is operating MHPPDs at a high reverse bias, which unfortunately leads to a higher I_d . It can deteriorate the detection limit (refers to the lowest level of X-ray radiation that can be reliably detected) and the dynamic range of the ionizing radiation response of a detector. Furthermore, due to their low defect formation energies, the formed defects within MHPs are prone to ion migration when subjected to an electric field. As a result, the high reverse bias applied to MHPPDs in ionizing radiation applications can trigger a saturation period lasting hours, referred to as I_d drift, which affects the current long-term stability of MHPPDs, as these devices are typically operated at a specific reverse bias voltage relative to the reference I_d .¹³ The I_d drift can be calculated using: $D = \frac{I_{\text{final}} - I_{\text{begin}}}{tE}$, where I_{final} and I_{begin} are the final and initial dark currents, t is the test time, and E is the applied electric field.

Therefore, understanding the fundamental causes of I_d in MHPPDs is crucial. By exploring the elements that influence I_d , we can devise effective strategies to mitigate it, thus overcoming the challenges associated with the material composition and device architecture. Although recent literature¹⁴ provides a thorough examination of I_d 's origins, limitations, and countermeasures in various MHP-based detectors like photodiodes, photoconductors, and phototransistors, there remains a gap concerning the specific issues of I_d in MHPPDs. Considering the significant impact of MHPPDs on the evolution of MHP-based photodetection technologies, further investigation in this area is essential. This review starts by defining the key performance metrics that are directly or indirectly influenced by I_d . It then examines the tunable MHP materials used in photodiodes, emphasizing their structural and morphological properties. We then explore the sources of I_d and identify the key factors influencing I_d in MHPPDs. Additionally, we discuss various tactics to curb I_d in these devices. Finally, we contemplate future approaches to reduce I_d in MHPPDs, underlining the necessity of developing a clear understanding of I_d 's mechanisms and exploring new avenues for research to diminish I_d effectively.

2. Figures of merits of photodiodes and their relationship with dark current

In the following section, we provide a comprehensive definition of the key performance metrics that are directly or indirectly influenced by I_d , thereby enabling a clear understanding of the reported MHPPD performances. A schematic illustration of several parameters affected by I_d is shown in Fig. 1. For the most relevant metrics, we highlight their definitions and mathematical expressions, as well as their relationships with I_d .

2.1 Signal-to-noise ratio

In photodiodes, the signal-to-noise ratio (SNR) is a measure of the quality of the signal relative to the level of background

noise. It is defined as the ratio of the photocurrent generated by the incident light (signal) to the noise current present in the system. Mathematically, the SNR can be expressed as:

$$\text{SNR} = \frac{i_{\text{ph}}}{i_n}$$

where i_{ph} is the photocurrent resulting from the incident light, and i_n is the total noise current. Since I_d contributes to the shot noise, which is a significant component of the total noise current, I_d directly affects the noise current and consequently impacts the SNR. A higher I_d results in increased shot noise, which reduces the SNR. Furthermore, for simplicity, the OOR is often employed to gauge the sensitivity of photodiodes to light signals. It is calculated as the ratio of the photocurrent to the I_d .

2.2 Spectral responsivity and EQE

The spectral responsivity (R) in units of A W^{-1} describes how much current is generated by a photodiode per incoming photon of a given energy. It can be calculated using the formula:

$$R = \frac{J_{\text{ph}}}{P_{\text{in}}}$$

where J_{ph} is the photocurrent density and P_{in} is the incident light intensity. EQE, which denotes the ratio between the number of incoming photons and the number of photogenerated free electrons, can be expressed as:

$$\text{EQE} = R \frac{h\nu}{q}$$

where h is the Planck constant, ν is the frequency of the incident photon, and q is the elementary charge. Generally, a high EQE (and hence R) is desirable to ensure efficient photon flux detection. In most cases, the EQE (or R) and I_d are considered independent parameters. However, it is important to note that a high I_d can lead to increased shot noise. This noise degrades the overall performance of the photodiode by making it more challenging to detect low-intensity signals accurately. This degradation can indirectly affect the effective EQE or (R) as well.

2.3 Speed

The speed of response, defined as the time required to collect photogenerated charge carriers at their respective contacts, ultimately determines the photodiode's dynamic range and cut-off frequency. Generally, the speed is evaluated based on the rise time (t_r) (the time it takes for the device response to increase from 10% to 90%) and the fall time (t_f) (the time it takes for the device response to decrease from 90% to 10%). The speed of response and I_d are both dependent on the intrinsic properties of the semiconductor materials, photodiode junction capacitance, and device operating temperature. For instance, high-quality semiconductors with fewer defects typically exhibit lower I_d and can also support faster response speeds. Conversely, high I_d can imply higher leakage in the junction, which may increase the junction capacitance.

Increased capacitance can slow down the response speed, as the photodiode takes longer to charge and discharge.

2.4 Noise equivalent power and specific detectivity (D^*)

The minimum incident light power that can be detected by a photodiode is referred to as the noise equivalent power (NEP). NEP is defined as the signal optical power that yields a SNR of 1. The NEP, expressed in units of $\text{W Hz}^{-1/2}$, can be calculated using the formula:

$$\text{NEP} = \frac{i_n}{R\sqrt{B}}$$

where i_n is the noise current and B is the detection bandwidth. The specific detectivity D^* in units of $\text{cm Hz}^{1/2} \text{W}^{-1}$ (or Jones) is the reciprocal of the NEP normalized to the square root of the device area A :

$$D^* = \frac{R\sqrt{AB}}{i_n}$$

As discussed, i_n primarily comprises shot noise, thermal noise, and flicker noise. Experimental measurements of i_n are challenging and not always performed. For simplicity, it is often assumed that the shot noise (i_{shot}) from the I_d is the dominant contribution to i_n :

$$D^* \cong \frac{R\sqrt{AB}}{i_{\text{shot}}} = \frac{R\sqrt{A}}{\sqrt{2qI_d}}$$

This assumption implies that the I_d (or i_{shot}) is the primary factor limiting D^* , while thermal noise and flicker noise are ignored. However, in photodiodes, and particularly in MHPPDs, i_n is not solely equivalent to i_{shot} , especially at low frequencies. Thus, this simplification can lead to an overestimation of D^* .

2.5 Linear dynamic range

In photodiodes, the linear dynamic range (LDR) is a specification that indicates the range of incident light intensities over which the photodiode can produce a linear (proportional) response in terms of the output photocurrent. Essentially, it quantifies the operational light intensity span of the image sensor. It is defined as the ratio between the maximum detectable photocurrent before saturation and the minimum detectable photocurrent above the noise floor. Mathematically, the LDR can be expressed in decibels (dB) as:

$$\text{LDR} = 10 \log \left(\frac{I_{\text{max}}}{I_{\text{min}}} \right)$$

where I_{max} is the maximum photocurrent that the photodiode can handle linearly, limited by the onset of saturation. I_{min} is the minimum photocurrent that can be detected above the noise floor, dominated by the I_d and other noise sources. A higher I_d increases the noise floor, thus raising the minimum detectable photocurrent I_{min} . Consequently, this reduces the LDR because: as I_{min} increases, the ratio $I_{\text{max}}/I_{\text{min}}$ decreases. This ratio determines the LDR, so an increase in I_{min} directly reduces the LDR.

3. Metal halide perovskites for photodiodes

Typically, MHPs have the general formula ABX_3 , where A represents monovalent cations such as CH_3NH_3^+ (MA), $\text{HC}(\text{NH}_2)_2^+$ (FA), cesium (Cs^+), and rubidium (Rb^+) or their combinations. B refers to divalent metal cations such as Pb^{2+} , Sn^{2+} , Bi^{2+} , and Ge^{2+} , while X represents halide anions such as Cl^- , Br^- , and I^- or a combination thereof. By adjusting the components, structure, and morphology, the optical absorption and electrical properties of MHPs can be easily modified. For example, as the ionic radius of the A cation increases ($r_{\text{Cs}^+} < r_{\text{MA}^+} < r_{\text{FA}^+}$), the lattice expands, and the bandgap decreases, leading to a red shift in the optical absorption band. Another way to tune the bandgap is by replacing Pb^{2+} with Sn^{2+} , which reduces the bandgap and extends the optical absorption edge into the near-infrared (NIR) region. Successive tuning of the bandgap of MHPs can also be manipulated by changing the halide composition. As shown in Fig. 2a, the halide composition changes from Cl^- to Br^- to I^- , and the bandgap sequentially decreases, allowing MHPs to absorb a broader range of light from ultraviolet (UV) to visible wavelengths.¹⁵ Furthermore, MHPs composed of Pb, Bi, I, and Br are promising for direct radiation detection due to the high atomic number of these elements, providing excellent potential for quick X-ray direct detection.¹⁶

The structure dimensionality of MHPs can be tuned from three-dimensional (3D) bulk materials to two-dimensional (2D) layered structures and one-dimensional (1D) chain materials by manipulating the connections of $[\text{BX}_6]^{4-}$ octahedral units (as shown in Fig. 2b). For instance, 2D MHPs are formed by incorporating larger organic cation layers between the octahedral network of 3D MHPs. This can be expressed as a general formula $(\text{LA})_m(\text{A})_{n-1}\text{B}_n\text{X}_{3n+1}$, where LA represents the larger organic cation and n denotes the number of layers in the 2D MHP structure. Introducing these larger organic cations in low-dimensional MHPs enhances their moisture stability and mechanical flexibility compared to their 3D counterparts. However, it should be noted that these long-chain organic cations also decrease the dielectric constant of MHPs, leading to an increase in the exciton binding energy. Consequently, the efficient separation and extraction of photogenerated carriers can be impeded.¹⁹

Moreover, the control over the morphology dimensionality of MHPs enables the incorporation of novel properties into these materials.²⁰ (Fig. 2b) For instance, 0D MHP nanostructures such as NCs and QDs exhibit tunable sizes ranging from several to tens of nanometers. These nanostructures generally possess large extinction coefficients and demonstrate characteristics of multiple-exciton generation. On the other hand, 1D MHP micro/nanostructures, including nanowires (NWs) and nanorods (NRs), feature significant surface-to-volume ratios and anisotropic geometries. These attributes contribute to low defect/trap densities, prolonged charge-carrier lifetimes, and reduced carrier recombination rates. Furthermore, 2D MHPs, comprising nanoplates, nanoflakes, and nanosheets,

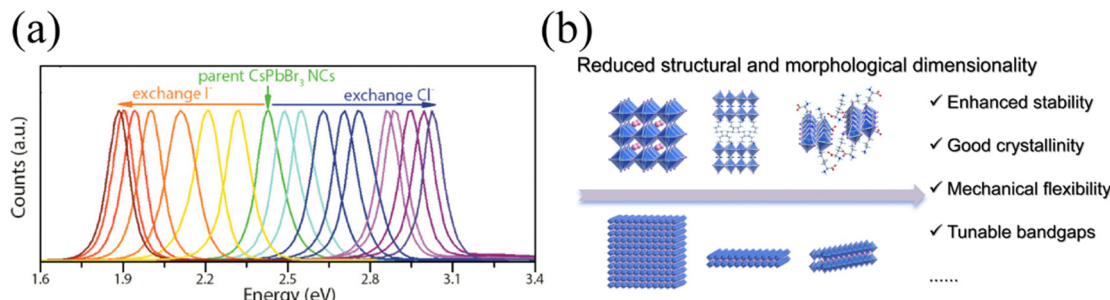


Fig. 2 (a) Bandgaps of MHPs (CsPbBr₃ nanocrystals) can be tuned by changing halide components. Reproduced with permission.¹⁷ Copyright 2015, ACS. (b) Optical and electrical properties can be tuned by the tunable dimensionality at the structural and morphological level of MHPs. Reproduced with permission.¹⁸ Copyright 2021, ACS.

exhibit strong quantum confinement effects and possess unique morphological characteristics. Additionally, these low-dimensional MHP materials demonstrate reasonable mechanical flexibility due to their atomic thickness. However, the nanostructures of low-dimensional MHPs still encounter issues that hinder charge transport and extraction in photodiodes. For instance, an excess of long-chain organic ligands on the surfaces of 0D and 2D MHPs can obstruct carrier transport, leading to reduced charge transfer efficiency. Moreover, the random orientation and rough morphology of 1D and 2D MHPs may create leakage paths, further impeding charge extraction. While 3D MHP polycrystalline materials have demonstrated remarkable improvements in photovoltaics due to their superior optoelectronic properties, overcoming challenges related to hysteresis and stability remains an ongoing endeavor.²¹

4. The origin of dark current in MHPPDs

4.1 Understanding dark current in MHPPDs

Typically, photodiodes are operated under reverse bias, so I_d is also known as reverse saturation current. In the following part, dark current density (J_d) is investigated by considering the device area in a photodiode. In photodiodes, J_d flow of majority carriers can be impeded by the interfacial barrier of P-N junctions. Thus, J_d in MHPPDs comprises several components: diffusion current (J_{diff}), influenced by thermodynamics; generation-recombination current ($J_{\text{g-r}}$), determined by various recombination processes such as trap-assisted recombination, Auger recombination, and radiative recombination; and tunneling current (trap assisted tunneling, TAT) and leakage current, influenced by traps present in the absorption layer and at the interface between the absorber materials or electrodes and subsequent transport layers, as shown in Fig. 3.

According to the following equation, J_{diff} of a semiconductor-based photodiode is determined by thermodynamics, such as the carrier density and bandgap of the materials used:

$$J_{\text{diff}} = qN_cN_v \left(\frac{1}{N_A} \sqrt{\frac{D_n}{\tau_n}} + \frac{1}{N_D} \sqrt{\frac{D_p}{\tau_p}} \right) \exp\left(-\frac{E_g}{k_B T}\right)$$

where D_p and D_n are the diffusion coefficients of holes and

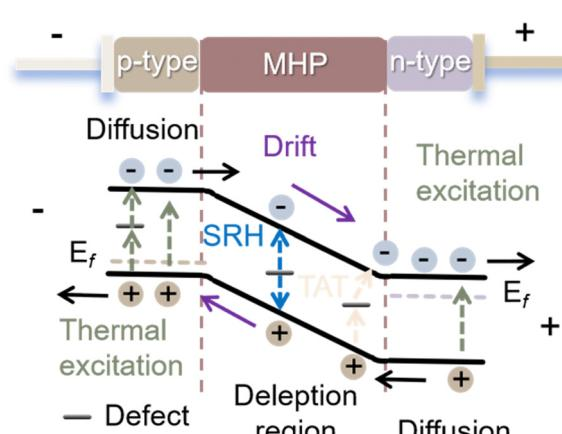


Fig. 3 The typical components and generation mechanisms of dark current in MHPPDs.

electrons, respectively. N_D and N_A represent the donor and acceptor concentrations on the n side and p side, respectively. N_c and N_v denote the effective density of states for electrons in the conduction band and holes in the valence band, respectively; τ_p and τ_n are the carrier lifetimes of holes and electrons, respectively. J_{diff} in a photodiode increases with temperature and decreases as the material quality increases.

The type of contact can influence J_{diff} . In the case of a Schottky contact, where the depletion region serves as the barrier layer, J_{diff} consists of various components. One of these components is the thermionic-emission current (J_T), which can be calculated using the Richardson-Dushman equation based on the thermionic-emission theory. This equation helps determine the contribution of thermionic emission to the overall J_{diff} .²²

$$J_T = AT^2 e^{-\frac{q\varphi_s}{kT}} \left(e^{\frac{qV}{kT}} - 1 \right)$$

The Richardson constant, denoted by A , has a value of 120 A (cm⁻² K⁻²) for vacuum. It reflects the relationship between the temperature, area, and the thermionic-emission current. The term $q\varphi_s$ represents the barrier height for carrier injection in the Schottky contact. Any changes in the Schottky barrier height (φ_s) affect J_T , the main contributor to J_{diff} in this contact.

configuration. On the other hand, in the case of an Ohmic contact where the depletion region acts as the accumulation layer, J_{diff} arises from a combination of carrier thermionic-emission and diffusion processes. Theoretically, introducing blocking layers with high enough barriers between materials and electrodes makes achieving low J_{diff} in the P–N junction possible.

Another significant source of J_{d} is the generation-recombination current ($J_{\text{g-r}}$), which arises from both the bulk depletion region and the interface. According to the Shockley–Read–Hall (SRH) model, $J_{\text{g-r}}$ is determined in the bulk layer:²³

$$J_{\text{g-r}} = \frac{qn_i X_{\text{d}}}{2\tau} \left(e^{\frac{qV}{2kT}} - 1 \right)$$

in addition to the factors mentioned earlier, $J_{\text{g-r}}$ depends on the intrinsic carrier concentration (n_i) and the non-equilibrium carrier lifetime (τ), which is inversely related to the trap concentration (N_t). $J_{\text{g-r}}$ is directly proportional to both N_t and the depletion region width (X_{d}). Unlike J_{T} , $J_{\text{g-r}}$ cannot be suppressed by the Schottky barrier alone. However, by reducing the concentration of traps in the semiconductor material, $J_{\text{g-r}}$ can be effectively suppressed. This highlights the importance of minimizing trap concentrations to achieve low J_{d} .

Aside from charge injection and bulk thermal generation of charge carriers, tunneling and leakage current processes also affect J_{d} in photodiodes. Photodiodes typically consist of multiple layers, including an absorber and a charge transport layer. Suppose traps are present in the absorber layer, in that case, trap-assisted tunneling can occur between the valence and conduction bands of the absorber materials or between the absorber materials and subsequent transport layers, increasing J_{d} .

4.2 Advancements in exploring dark current mechanisms in MHPPDs

In the context of MHPPDs, investigating the factors that influence J_{d} is essential for elucidating its origin. Researchers have identified that one of the primary origins of J_{d} in MHPPDs is the migration of ions through the bulk of the grains *via* point defects or extended defects, such as grain boundaries, which are considered material imperfections specific to MHPPDs. A study conducted by Jang *et al.* compared MHPPDs based on Pb and Sn MHP films. The researchers discovered that vertical grain boundaries in these materials contribute to increased J_{d} , while horizontal grain boundaries have the opposite effect of reducing J_{d} .²⁴ This disparity can be attributed to smaller grains in the Sn-based MHPs, resulting in divergent shunt pathways for J_{d} . (Fig. 4a) Consequently, Yang *et al.* conducted a study in which they observed a decrease in the J_{d} of MHP films containing potassium salt additives by reducing the crystal grain size of Sn-based MHPs. This reduction in J_{d} was attributed to the increased presence of shunting paths.²⁵ Furthermore, the inherently weaker halide-ion migration in the Sn-based material provides an advantage in suppressing J_{d} . Similarly, Dey *et al.* conducted an investigation using scan-rate-dependent hysteresis analyses, temperature-dependent impedance spectroscopy measurements, and first-principles calculations

on mixed Pb–Sn MHPs.²⁶ Their research revealed the crucial role of Sn vacancies in enhancing the migration barrier of iodide ions, which occurs due to local structural distortions. Yin *et al.* conducted a study highlighting the significant contribution of surface iodine vacancies to J_{d} in polycrystalline MHPPDs.²⁷ Their experimental findings revealed that the trap states induced by surface iodine vacancies within the bandgap can create many generation and recombination centers. Consequently, this leads to a decrease in the minority carrier lifetime and an increase in the generation–recombination current density based on the SRH mechanisms under dark conditions (Fig. 4b). Moreover, Moseley *et al.* underscored the significance of considering the presence of defects in MHP films, which can result in J_{d} that exhibit time-dependent drifting over seconds, as they can cause measurement challenges such as speed and LDR.²⁸ These defects and trap states can generate a photoconductive gain by extending carrier lifetimes beyond transit times or altering interface energetics, enabling charge injection even under low light intensity in MHPPDs.

In addition to the presence of structural and compositional imperfections such as pinholes, trap states, and grain boundary leakage in MHPs, the contact between the MHPs and the charge transport layers (CTLs) or electrodes also significantly influences the experimental J_{d} of MHPPDs. Sutherland *et al.* observed that MHPPDs and MHP-based solar cells exhibit differences in their reverse saturation current density.³¹ Given

$$\text{that } V_{\text{oc}} = nKTq^{-1} \ln \left[\frac{\left(J_{\text{sc}} - \frac{V_{\text{oc}}}{R_{\text{sh}}} \right)}{J_0} + 1 \right], \text{ shunt paths are not}$$

crucial in limiting V_{oc} (open-circuit voltage) until R_{sh} (shunt resistance) becomes extremely small. Shunt paths of this magnitude can immensely increase J_{d} under reverse bias. Thus, it is not always guaranteed that the efforts to optimize solar cell performance will result in sufficiently low J_{d} for effective photodetection. They further developed the electron contact composites ($\text{TiO}_2/\text{Al}_2\text{O}_3/\text{PCBM}$) for MHPPDs to minimize J_{d} . Duijnsteet *et al.* discovered that the experimental data must consider an interface injection barrier to fit the TPC measurement.³² They pointed out that the injection barrier and ionization of trapped carriers at the interface contribute to the J_{d} . Moreover, Ollearo *et al.* demonstrated that the interfacial energy offset between the electron-blocking layers and the MHPs significantly determines the magnitude of J_{d} .²⁹ As the offset increases, it can efficiently suppress the thermal charge generation at the interface between electron-blocking layers (EBL) and the MHPs, leading to a significantly lower J_{d} (Fig. 4c).

4.3 The dark current drift in MHPPDs

The J_{d} ’s saturation period under reverse bias conditions commonly known as instabilities in the dark reverse saturation current can lead to measurement inaccuracy in MHPPDs, especially for direct radiation detection. It is worth mentioning that other halide-based radiation detectors under the high

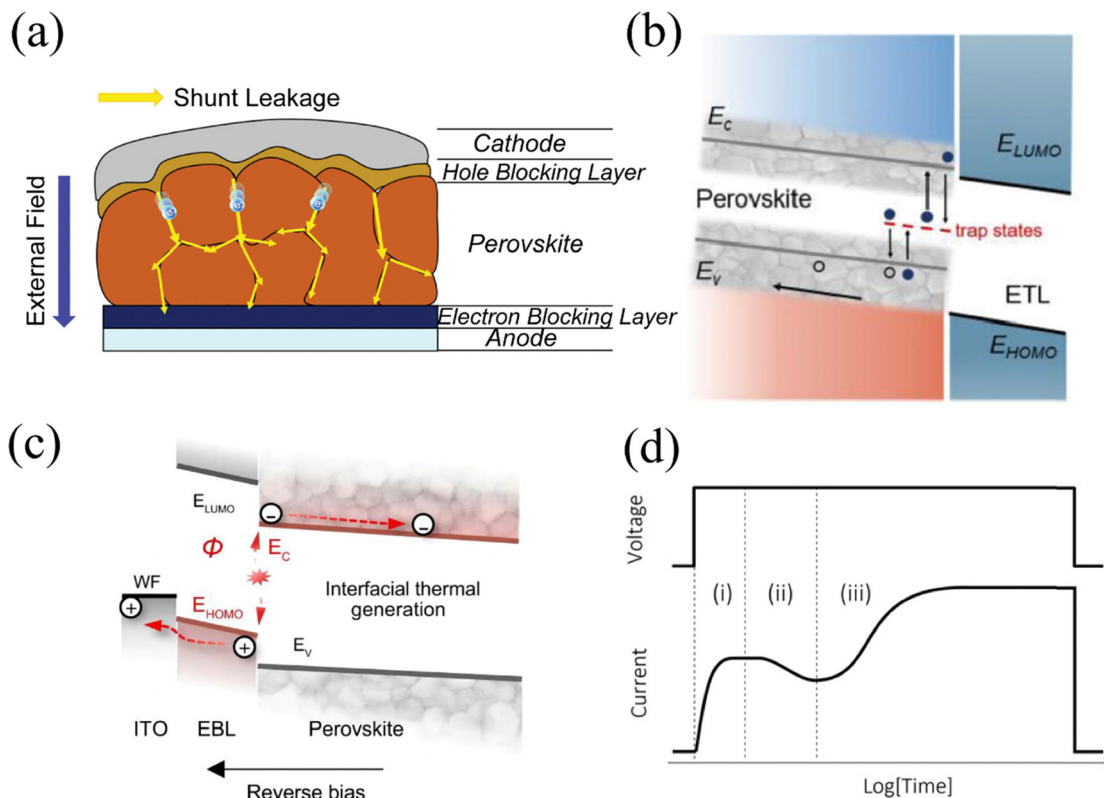


Fig. 4 (a) Diagram illustrating the formation of multiple divergent leakage pathways in a Sn-based MHP with a reduced grain size. Reproduced with permission.²⁴ Copyright 2022, Wiley-VCH. (b) Schematic energy level diagram showing the generation–recombination processes enhanced by surface trap states under dark conditions. Reproduced with permission.²⁷ Copyright 2023, Wiley-VCH. (c) Schematic representation of the thermal charge generation mechanism at the EBL-MHP interface. Reproduced with permission.²⁹ Copyright 2021, Nature. (d) Schematic regime of long-term dark reverse bias current response for MHPPDs. Reproduced with permission.³⁰ Copyright 2022, Wiley-VCH.

reverse bias conditions also face the problem of J_d drift.³³ Recent studies have highlighted two leading causes for the J_d drift in MHP films used in direct radiation detection. Firstly, the presence of mobile ions within the bulk and grain boundaries of MHP films can contribute to the drift.³⁴ Secondly, the trapping or accumulating charge carriers at interlayers can also lead to the drift phenomenon. Several techniques and models have been employed to investigate and predict the transient J_d decay characteristics associated with the trapping or accumulating charge carriers at interlayers. Different MHP absorbers and interlayer materials have been studied in this regard.^{35–37}

Understanding the ionic conduction in MHPs, in terms of electronic and ionic behaviors, is crucial in comprehending the J_d drift regarding ion migration process. Yang *et al.* studied $\text{MA}_{1-x}\text{FA}_x\text{PbI}_3$, a mixed electronic/ionic material, they discovered that halide (iodine) migration occurs under an electric field in such materials by measuring and modeling the stoichiometric polarization by the mixed conduction.³⁸ Investigating ion mobility in different MHPs is significant due to their known halide ion-conducting properties under dark conditions. García-Batlle *et al.* conducted a comparative analysis of two compounds, namely MAPbBr_3 and MAPbI_3 , along with different structures, such as single-crystalline and microcrystalline, to study the long-term evolution of J_d .³⁹ To estimate the ion mobility in these systems, they employed ionic time-of-

flight measurement techniques and obtained values ranging from 10^{-7} to $10^{-6} \text{ cm}^2 \text{ V}^{-1} \text{ s}^{-1}$. The results revealed that bromide compounds exhibited lower ion mobility, dependent on the electric field. Conversely, iodide compounds showed higher ion mobility, independent of the electric field. In addition, Almora *et al.* performed MATLAB code driftfusion simulations to investigate the long-term reverse bias current behavior in MHPPDs.³⁰ (Fig. 4d) Their findings revealed that the steady-state J_d observed under reverse bias is primarily an electronic current rather than an ionic current, even though the presence and concentration of mobile ions play a crucial role. The reduction of J_d drift through screening is influenced by the following factors: the thickness of the MHPs, the applied electric field, the concentration of mobile ions, and the mobile ion mobility. By employing material engineering techniques such as composition and interface engineering in MHPs, it is possible to reduce the screening of J_d drift.

5. Strategies for suppressing dark current toward high performance MHPPDs

Comprehending the components and underlying mechanisms of J_d in photodiodes is crucial for understanding their operational behavior. This knowledge facilitates the development of

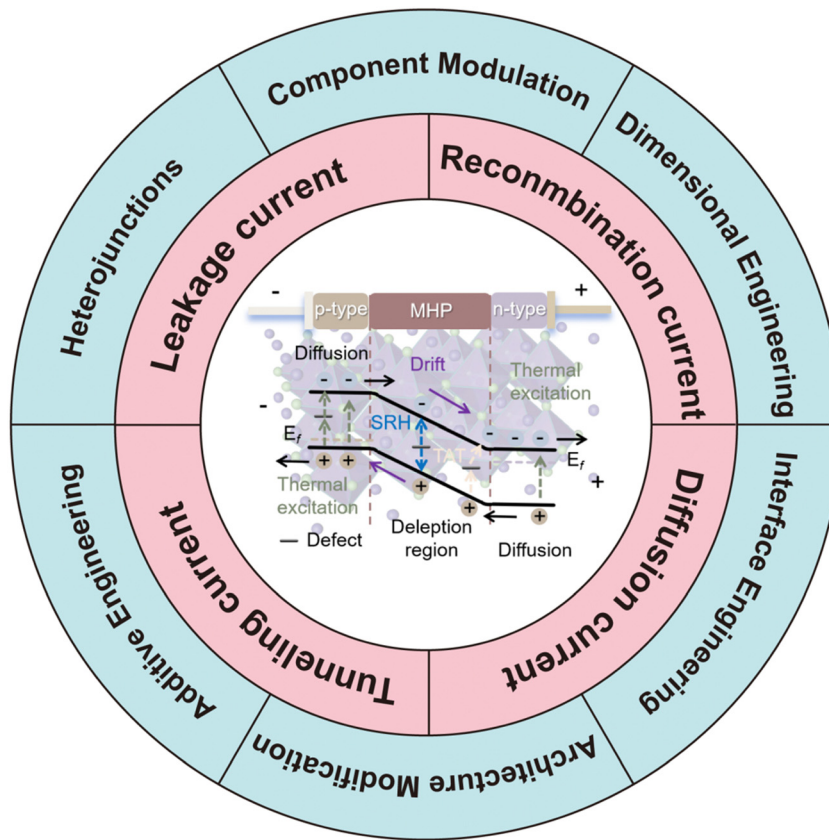


Fig. 5 Schematic illustration of the components of J_d and the methods for suppressing the J_d of MHPPDs.

targeted strategies to mitigate J_d in MHPPDs. For instance, operating these devices at lower temperatures can effectively reduce the intrinsic carrier concentration within the MHP film, which serves to suppress J_{diff} . Additionally, employing techniques such as compositional modulation and bulk passivation can enhance the MHP film quality and reduce inherent material defects, thereby diminishing J_{g-r} . Furthermore, employing interfacial engineering strategies, including the use of insertion layers or passivation techniques, can crucially curb surface or interfacial defects. This, in turn, helps to decrease J_d associated with trap-induced carrier generation and recombination. The application of heterojunctions allows for the integration of MHP with other materials, promoting optimal band alignment, reducing surface defects, and tuning related optical and electrical properties. Such alignment, aided by the built-in potential, acts as a barrier against the flow of majority carriers to decrease J_{diff} . Moreover, modifications in device architecture can influence carrier transport mechanisms and promote band bending, which further prevents carrier recombination. In the following section, we delineate comprehensive strategies for mitigating J_d in both the material composition and device structure to boost performance and ensure the reliability of optoelectronic applications, as shown in Fig. 5.

5.1 Component modulation

As ionic crystals, MHPs exhibit formation energies for anion/cation vacancies that are largely influenced by Coulomb

interactions between the ions and crystal frameworks. By precisely controlling the composition of MHP crystals, it becomes feasible to enhance bonding energy, alleviate stress, optimize morphology and crystallinity, and significantly decrease J_d .

For instance, as shown in Fig. 6(a)–(c), Yun *et al.* investigated the engineering of A-site monovalent cations in wide-bandgap MHPs for high-performance blue photodetection.⁴⁰ Their findings revealed that introducing FA in MA increased the heat of formation, leading to modulated nucleation and grain growth behavior. Furthermore, the incorporation of optimal Cs (5%) helped mitigate strain and decrease trap states in the MHP thin film, resulting in a more compact and better-arranged crystal lattice. These improvements enabled the fabrication of N-I-P devices with a decent D^* of 5.08×10^{12} Jones, and demonstrated the feasibility of individual 7×7 devices for real image sensing under 450 nm blue light illumination. Additionally, Liu *et al.* explored the modulation of A-site monovalent cations and X-site halide anions in MHPPDs for direct X-ray detection.⁴¹ They observed that smaller cations (MA^+ and Cs^+) and anions (Br^-) resulted in the release of lattice stress and improved morphology, as evidenced in Fig. 6d. The optimized composition of $\text{FA}_{0.85}\text{MA}_{0.1}\text{Cs}_{0.05}\text{PbI}_{2.55}\text{Br}_{0.45}$ exhibited superior properties, including an ultra-low trap density of $(4.6 \pm 2.4) \times 10^9 \text{ cm}^{-3}$, a long carrier lifetime of $6.4 \mu\text{s}$, and a diffusion length of $68.9 \mu\text{m}$. This composition achieved an extremely low J_d of $-1.44 \mu\text{A cm}^{-2}$ at -75 V bias, and a low detection limit of $42 \text{ nGy}_{\text{air}} \text{ s}^{-1}$. Furlan *et al.* demonstrated the tunable halide

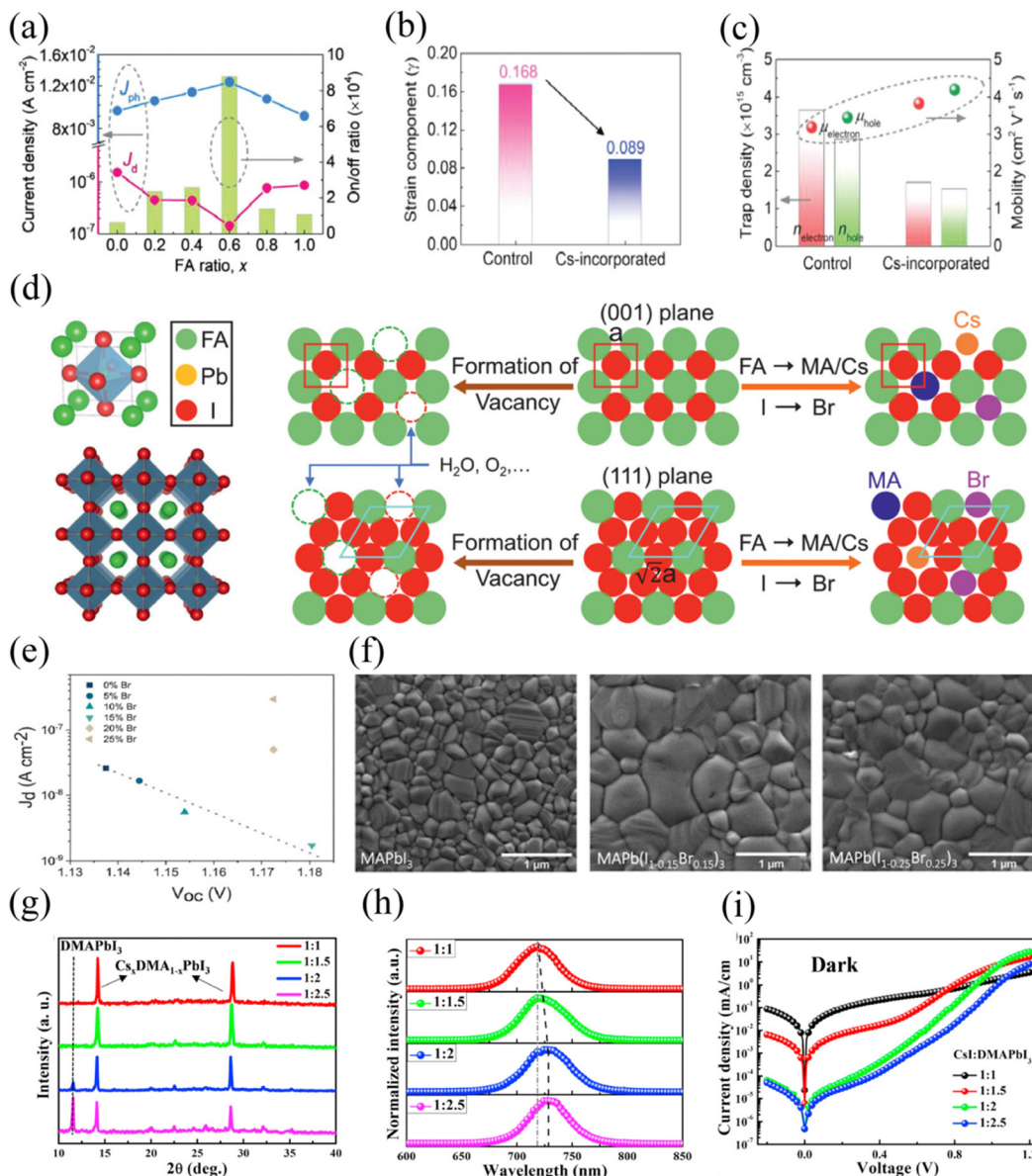


Fig. 6 (a) J_d , and photocurrent density, and on/off ratio with the different FA/MA ratios. (b) Strain components of control and Cs-incorporating MHP films. (c) Trap density and mobility of control and Cs-incorporating MHP films obtained from the electron/hole-only configuration. Reproduced with permission.⁴⁰ Copyright 2022, Wiley-VCH. (d) Schematic illustration of the lattice stress release of the 3-cation mixed-halide FAMACs MHPs. Reproduced with permission.⁴¹ Copyright 2020, Wiley-VCH. (e) The relationship between J_d and V_{oc} with various halide Br and I ratios. (f) Surface morphology of $\text{MAPb}(\text{I}_{1-x}\text{Br}_x)_3$ MHP thin films obtained by scanning electron microscopy. Reproduced with permission.⁴² Copyright 2022, Wiley-VCH. (g) and (h) XRD patterns and PL spectra of the $\text{Cs}_x\text{DMA}_{1-x}\text{PbI}_3$ films. (i) $J-V$ curves of MHPPDs in the dark based on the $\text{Cs}_x\text{DMA}_{1-x}\text{PbI}_3$ films. Reproduced with permission.⁴³ Copyright 2020, Elsevier.

composition in organic cation-based MHPs.⁴² By adding Br to MAPbI_3 -based MHPs, they not only adjusted the bandgap through lattice contraction but also reduced non-radiative recombination losses in MHP layers by tuning the crystallite size, as shown in Fig. 6f. They established a correlation between the reduced J_d ($1.3 \times 10^{-9} \text{ A cm}^{-2}$ at -0.5 V), V_{oc} enhancements (Fig. 6e), and achieved high-performance MHPPDs (D^* of $8.7 \times 10^{12} \text{ Jones}$) within the range of 350–850 nm. Although inorganic MHPs (CsPbX_3) are suitable for high-performance and stable photodetection applications, they also exhibit

thermodynamic instability at room temperature and spontaneously transform into a photo-inactive phase under ambient conditions due to the small tolerance factor. Li *et al.* demonstrated high-performance MHPPDs with an ultra-low J_d ($6.4 \times 10^{-5} \text{ mA cm}^{-2}$) (Fig. 6i) and a high speed of 558 ns by utilizing the organic cation DMA ($\text{DMA}^+ = \text{dimethylammonium, } (\text{CH}_3)_2\text{NH}_2^+$) to enhance the room-temperature phase stability of Cs-based MHP thin films.⁴³ The blue shift of the diffraction peak position observed in Fig. 6g was attributed to the introduction of DMA^+ , which has a larger ionic size than Cs^+ . In

addition, this finding was supported by the photoluminescence spectra (PL) of the Cs^+ and DMA^+ -based MHP films.

In addition to the effective modulation of A-site and X-site components to reduce J_d and improve device performance, researchers have also been exploring B-site regulation. For instance, hybrid Pb-Sn MHP-based MHPPDs have been investigated to achieve a broad spectral response ranging from 300 nm to 1000 nm, while also reducing J_d compared to Pb-based devices, thanks to the reduced trap density.⁴⁴ Furthermore, researchers have conducted halide composition modulation to develop non-toxic bismuth MHPs.⁴⁵ All of these demonstrations highlight the significant potential of component modulation in MHPs for effectively suppressing J_d and enhancing device performance. An update on the progress in the reported component modulation of the MHPPDs is provided in Table 1.

5.2 Dimensional engineering

Numerous studies have shown that effective dimensional regulation of MHPPDs using hydrophobic organic cations can reduce the dimension of MHPs and transition them from 3D to quasi-2D structures. This not only helps suppress defects, thanks to the high defect formation energies of quasi-2D MHPs, but also significantly improves their stability. Thus, efforts have focused on creating a quasi-2D MHP layer at the interface, forming a 2D/3D MHP structure.^{27,53-55} This

approach leads to fewer trap states at the MHP and electrode interface, consequently improving device performance. However, it is important to note that excessive presence of 2D MHPs at the interface, as well as disordered phase distribution, can impede charge transport due to the insulating effect of the bulkier, long-chain organic spacer cations (as illustrated in Fig. 7a). Recent efforts have therefore aimed at creating uniformly distributed, compact 2D–3D gradient MHPs with an ordered phase distribution along the thin film's longitudinal direction, as this offers enhanced optoelectronic properties, stability, and ideal MHPPD characteristics. For instance, Miao *et al.* employed the hot-casting method to control the phase distribution of quasi-2D MHP thin films.⁵⁶ By comparing the top and bottom PL spectra of different MHP thin films (as shown in Fig. 7b), they studied the effects of substrate temperature on surface morphology and internal phase distribution. The resulting device showed an extremely low J_d ($2.3 \times 10^{-11} \text{ A cm}^{-2}$), large D^* at 455 nm ($1.22 \times 10^{14} \text{ Jones}$), ultra-fast speed (5.5/4.7 μs), and remarkable stability. Additionally, Peng *et al.* reported an ion-exchange strategy to prepare 2D–3D thick MHP films with uniform morphology, vertically aligned monolithic crystal phases, and reproducibility (as shown in Fig. 7c).⁵⁷ By performing an ion exchange between Br^- and I^- halide anions, they achieved a slow crystallization process resulting in a gradient phase distribution of 2D–3D MHP thick films. *In situ*

Table 1 Summary of the component modulation in bulk MHPs for suppressing J_d and enhancing the FOMs of MHPPDs

Strategy	Device structure	Dark current (density) (I_d or J_d)	D^* (Jones)	Speed [rise time (t_r)/ LDR fall (decay) time (t_f)] (dB)	Ref.
Reduce bulk defects (rubidium incorporated into FAPbI_3)	ITO/PEDOT:PSS/MHP/ C_{60} /BCP/Cu	$10^{-10} \text{ A cm}^{-2}$ (0 V, about 100 times reduced)	1.7×10^{12}	300—ns	125 46
Alleviate stress and reduce bulk defects (Cs incorporated into FAPbI_3)	ITO/MeO-2PACz/MHP/ C_{60} /BCP/Ag	$3.3 \times 10^{-9} \text{ A cm}^{-2}$ (−0.5 V)	6.1×10^{11}	1.2/1.2 μs	135 47
Optimize morphology and crystallinity (Cs and Br optimization in FAPbI_3)	ITO/ MoO_3 /TaTm/MHP/ C_{60} /CN-T2T: C_{60} /Ag	$8.627 \times 10^{-10} \text{ A cm}^{-2}$ (0 V)	1.747×10^{13} (530 nm)	629/616 ns	127 48
Alleviate stress and reduce bulk defects (Cs , MA , FA optimization in APbBr_2Cl)	ITO/ SnO_2 /MHP/PMMA/Spiro-OMeTAD/Au	$3.04 \times 10^{-8} \text{ A cm}^{-2}$ (0 V)	5.57×10^{12}	585/531 μs	— 40
Optimize morphology and crystallinity (Br , Cl , I optimization in MAPbX_3)	ITO/ SnO_2 /MHP/Spiro-OMeTAD/Au	$2.7 \times 10^{-7} \text{ A cm}^{-2}$ (0 V)	8.65×10^{11}	2.35/2.87 ms	— 49
Optimize morphology and crystallinity (Br , I optimization in $\text{Cs}_x\text{Bi}_2\text{I}_{9-x}\text{Br}_x$)	ITO/PEDOT:PSS/MHP/ C_{60} /BCP/Ag	$3.5 \times 10^{-9} \text{ A cm}^{-2}$ (0 V)	4.6×10^{11} (410 nm)	40.7/27.1 ms	— 45
Reduce bulk defects (FA incorporated into MAPbI_3)	ITO/PTAA/MHP/ C_{60} /BCP/Cu	$0.02 \text{ pA Hz}^{-1/2}$ (noise signal) ^a (0 V)	$27.7 \text{ nGy}_{\text{air}} \text{ s}^{-1}$ (detection limit) ^b	86/500 μs	— 50
Reduce bulk defects and increase film thickness (Cs , DMA optimization in $\text{Cs}_x\text{DMA}_{1-x}\text{PbI}_3$)	ITO/PTAA/PMMA/MHP/PCBM/Bphen/Cu	$6.4 \times 10^{-5} \text{ mA cm}^{-2}$ (−0.2 V, about 10^3 times reduced)	Over 1.0×10^{13}	558 ns (TPC extracted) ^c	— 43
Optimize morphology, reduce bulk defects (Br , Cl optimization in $\text{CsPbBr}_x\text{Cl}_{3-x}$)	ITO/MHP/Au	$10^{-8} \text{ A cm}^{-2}$ (0 V)	10^{12}	75/70 μs	137 51
Alleviate stress and reduce bulk defects (Cs , MA , FA and Br , I optimization in MHPs)	Au/BCP/ C_{60} /MHP/SpiroTTB/Au	$-1.44 \mu\text{A cm}^{-2}$ (−75 V)	$42 \text{ nGy}_{\text{air}} \text{ s}^{-1}$ (detection limit) ^b	2.3/57.2 μs	— 41
Optimize morphology (FA , and Sn optimization in MHPs)	ITO/PEDOT:PSS/MHP/ C_{60} /BCP/Ag	$5.2 \times 10^{-8} \text{ A cm}^{-2}$ (−0.2 V)	10^{12}	6.9/9.1 μs	167 52
Optimize morphology and reduce bulk defects (Br , I optimization in $\text{MAPbBr}_3\text{I}_x$)	ITO/MeO-2PACz/MHP/PCBM/BCP/Cu	$1.3 \times 10^{-9} \text{ A cm}^{-2}$ (−0.5 V, about 20 times reduced)	8.7×10^{12}	0.58/0.17 μs	133 42

^a Noise signal: the noise signal in photodetection is recorded by utilizing a fast Fourier transform signal analyzer combined with a preamplifier to capture the noise current at various frequencies. ^b Detection limit: the detection limit in X-ray detection is defined as the equivalent dose rate to produce a photocurrent greater than three times the noise current (dark current). ^c TPC extracted: speed here can be defined as the time at which the photocurrent decays from the peak to the original 1/e extracted from the transient photocurrent curves.

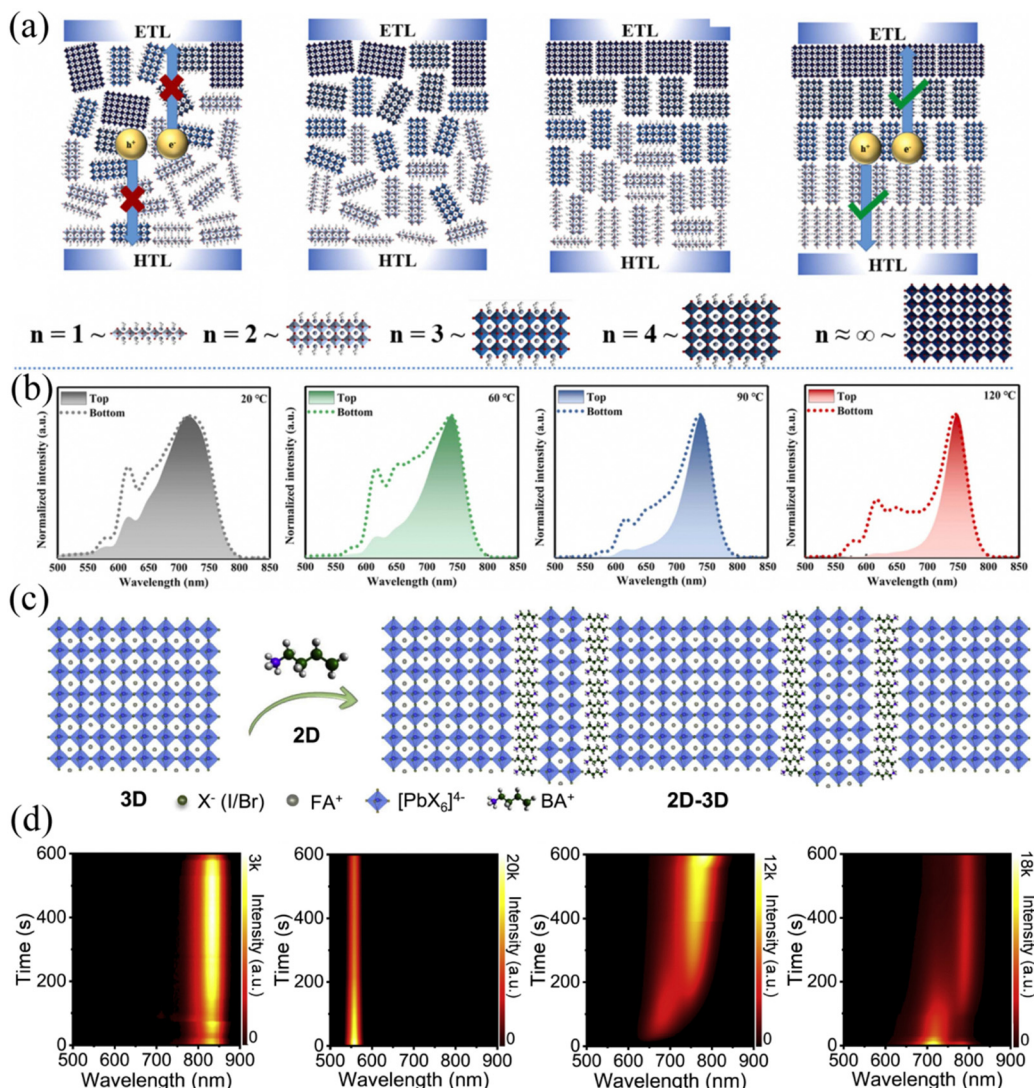


Fig. 7 (a) Schematic diagram of the internal phase arrangement process and the corresponding charge transportation in MHP thin films. (b) The top and bottom PL spectra of different phase arrangement films. Reproduced with permission.⁵⁶ Copyright 2023, Elsevier. (c) Schematic illustration of the self-assembled 2D–3D MHPs obtained by an ion-exchange-induced crystallization method. (d) PL spectra monitoring of different 2D–3D MHP combinations.⁵⁷ Reproduced with permission. Copyright 2022, Elsevier.

PL spectra monitoring helped unveil the effect of halide anions (Br^- and I^-) on crystal formation in these thick MHP films (Fig. 7d). The resulting 2D–3D MHP thick film-based devices exhibited extremely low J_d (0.8 nA cm^{-2}), an ultra-fast speed of 640 ns, and a detection limit of $4.2 \text{ nGyair s}^{-1}$. Furthermore, they demonstrated a prototype 1024-pixel detector array for X-ray imaging. The strategies and the corresponding device structures and performance parameters are summarized in Table 2. These advancements in engineering the dimensional and phase distribution of MHPs hold great promise for achieving high-performance and stable MHPPDs.

5.3 Additive engineering and the modulation of crystallization methods

Being an ionic crystal, the occurrence of anion/cation vacancies within the bulk and at the interface of MHPs is inevitable

during the thin film formation process. To address this, a passivation technique involving the addition of additives in the bulk and at the interface of MHPs has been developed. This technique creates coordinating bonding, eliminates vacancies, and fills interstitial spaces, ultimately leading to a reduction in J_d of the MHPPDs. We have summarized the progress in MHPPDs achieved through the application of relevant additive engineering for both the bulk and interface of MHPs in Table 3.

For instance, Wang *et al.* devised a moisture-triggered additive, poly(vinyl alcohol) (PVA), to passivate surface defects in FAPbI_3 .¹⁰⁴ Their results demonstrate that the PVA organic framework fills the grain boundaries of FAPbI_3 , thereby stabilizing the favorable black phase of FAPbI_3 and guarding against moisture intrusion through strong interactions with water molecules. The PVA-passivated FAPbI_3 films also exhibit self-healing capabilities upon bending, activated by water

Table 2 Summary of the dimensional engineering in MHPs for suppressing J_d and enhancing the FOMs of MHPPDs

Strategy	Device structure	Dark current (density) (I_d or J_d)	D^* (Jones)	Speed [rise time (t_r)/fall (decay) time (t_f)]	LDR (dB)	Ref.
Regulate band alignment (quasi 2D (BDA _{0.7} (BA ₂) _{0.3})(EA) ₂ Pb ₃ Br ₁₀ MHPs)	ITO/bl-TiO ₂ /mp-TiO ₂ /MHPs/PTAA/Au	2.65×10^{-12} A (0 V)	2.5×10^{15}	270/920 μ s	—	58
Regulate band alignment (2D/3D (BzA) ₂ MA _{n-2} Pb _n I _{3n+1} /MAPbI ₃)	ITO/bl-TiO ₂ /mp-TiO ₂ /MHPs/PTAA/Au	8.32×10^{-10} A cm ⁻² (0 V, about 1.79 times reduced)	1.21×10^{13}	53/38 μ s	—	59
Optimize morphology and reduce bulk defects (quasi 2D (BA) ₂ MA ₃ Pb ₄ I ₁₃)	ITO/PEDOT:PSS/MHP/PCBM/BCP/Ag	2.3×10^{-11} A cm ⁻² (0 V)	1.22×10^{14}	5.5/4.7 μ s	173.4	56
Optimize morphology and crystallinity, reduce bulk defects (quasi 2D PEA ₂ MA ₄ Pb ₅ I ₁₆)	ITO/PEDOT:PSS/MHP/BCP/Ag	0.36 pA Hz ^{-1/2} (noise signal) ^c (0 V)	1.4×10^{12}	64/162 μ s	120	60
Regulate band alignment (quasi 2D (BA) ₂ MA ₄ Pb ₅ I ₁₆)	ITO/PTAA/MHP/C ₆₀ /BCP/Ag	5×10^{-9} mA cm ⁻² (0 V)	7×10^{12} (600 nm)	1.48/1.58 μ s	> 200	61
Regulate band alignment (quasi 2D (PEA) ₂ (MA) ₅₉ Pb ₆₀ I ₁₈₁)	FTO/TiO ₂ /MHP/Spiro-OMeTAD/Au	1.76×10^{-7} A cm ⁻² (0 V)	2.20×10^{12} (750 nm)	1.59/0.02 s	41	62
Reduce surface defects and increase crystallinity (2D/3D/2D PEA ₁ /Cs _{0.05} MA _{0.45} FA _{0.5} Pb _{0.5} Sn _{0.5} I ₃ /PEAI)	ITO/PTAA/PEAI/MHP/PEAI/C ₆₀ /BCP/Cu	1.25×10^{-3} mA cm ⁻² (-0.1 V)	2.07×10^{11} (910 nm)	35 ns TPC extracted ^a	—	54
Alleviate stress and reduce bulk and interface defects (2D/3D (PTABr and PEABr)/tri-cation MHPs)	ITO/PEDOT:PSS/MHP/PCBM/Ag	—	10^{12} (730 nm)	40 μ s TPC extracted ^a	—	53
Optimize morphology and crystallinity (quasi 2D (BA) ₂ MA _{n-2} Pb _n I _{3n+1})	ITO/PTAA/MHP/C ₆₀ /BCP/Au	10^{-5} mA cm ⁻² (3 kV cm ⁻¹)	—	—	—	63
Optimize morphology and crystallinity (2D-3D (BA ₂ PbBr ₄) _{0.5} FAPbI ₃)	ITO/NiO _x /PEIE/MHP/C ₇₀ /BCP/Au	0.8 nA cm ⁻²	4.2 nGy air s ⁻¹ (detection limit) ^b	640 ns/—	—	57
Regulate band alignment, optimize morphology and crystallinity and reduce surface defects (2D/3D PEAI/MAPbI ₃)	ITO/SnO ₂ /MHP/PTAA/Au	$\sim 3.1 \times 10^{-14}$ A Hz ^{-1/2} (noise signal) ^c (0 V, about 1.8 times reduced)	2.57×10^{12} (740 nm)	1.7/9.8 μ s	161	55
Optimize morphology and crystallinity (2D-3D (PA ₂ PbI ₄) _x (FA _{0.83} Cs _{0.17} PbI ₃) _{1-x})	ITO/PTAA/PEIE/MHP/C ₆₀ /BCP/Cu	7 fA Hz ^{-1/2} (noise signal) ^c (-0.5 V)	3.7×10^{13}	< 80 ns	182	64
Optimize morphology and reduce bulk and surface defects (quasi 2D PEA ₂ MA ₃ Pb ₉ I ₂₈)	ITO/MHP/Au	1.8×10^{-2} pA cm ⁻² s ⁻¹ V ⁻¹ (drifting) ^d	69 nGy _{air} s ⁻¹ (detection limit) ^b	—	—	65
Reduce surface defects (2D/3D PEA ₂ PbBr ₄ /MAPbI ₃)	ITO/MHP/Au	2.6×10^{-10} A cm ⁻² (0.5 V mm ⁻¹)	10.17 nGy _{air} s ⁻¹ (detection limit) ^b	228/197 μ s	—	66
Reduce surface defects (2D/3D BAI/MAPbI ₃)	ITO/NiO _x /MHP/PCBM/Bphen/Ag	3.78×10^{-10} A cm ⁻² (-0.1 V)	1.46×10^{12}	1.03/3.20 μ s	—	27
Regulate band alignment (quasi 2D (PEA) ₂ MA ₃ Pb ₄ I ₁₃)	ITO/MHP/PCBM/Ag	0.4 nA (0 V)	3.38×10^{12} (570 nm)	20.8/20.6 μ s	99.6	67

^a TPC extracted: speed here can be defined as the time at which the photocurrent decays from the peak to the original 1/e extracted from the transient photocurrent curves. ^b Detection limit: the detection limit in X-ray detection is defined as the equivalent dose rate to produce a photocurrent greater than three times the noise current (dark current). ^c Noise signal: the noise signal in photodetection is recorded by utilizing a fast Fourier transform signal analyzer combined with a preamplifier to capture the noise current at various frequencies. ^d Drifting: drifting means the dark current drift period D .

molecules (Fig. 8a). Ionic liquids serve as promising candidates for bulk defect passivation in MHPs due to their diverse controllable sources of anions and cations. Gao *et al.* showcased the effectiveness of 1-butyl-2,3-dimethylimidazolium chloride (BMIMCl) in passivating defects within CsSnI₃ NW-based films.⁹⁵ Their study revealed that BMIMCl exerts a potent passivating effect on Sn-related defects through the large π -bonds in N=C=N, enhancing electron density around Sn²⁺ in CsSnI₃ and shielding it from oxidation to Sn⁴⁺. By combining polymethyl methacrylate (PMMA) for bulk defect passivation in CsSnI₃ NW-based films, the CsSnI₃-based MHPPDs demonstrated reduced J_d and highly stable behavior (Fig. 8b).

Thiocyanate salts are recognized as effective additives for controlling the crystallization process and delaying oxidation through strong interactions with metal cations. Liu and colleagues investigated the impact of multifunctional tin thiocyanate (Sn(SCN)₂) additives on Sn-Pb MHPs.¹⁰⁰ Their addition of the additive to the Sn-Pb MHP precursor led to a preferred double-sided surface distribution within the MHP film, effectively reducing Sn oxidation levels (Fig. 8c). Subsequently, they achieved a high D^* (8.48×10^{12} Jones at 910 nm) and outstanding stability (lifetime of 2300 h) in NIR MHPPDs. Effective additives in the bulk of quasi-2D MHPs can regulate the 3D MHP phase within quasi-2D MHP films. Di *et al.* introduced

Table 3 Summary of additive engineering and the modulation of crystallization methods for bulk and interface of MHPs to suppress J_d and enhance FOMs of MHPDs

Strategy	Device structure	Dark current (density) (I_a or J_d)	D^* (Jones)	Speed [rise time (t_r)/fall (decay) time (t_f)]	LDR (dB)	Ref.
Optimize morphology and crystallinity (Mn doped into $\text{Cs}_3\text{AgBiBr}_6$)	ITO/SnO ₂ /MHP/Ag	—	3.46×10^{-10} (405 nm) 3.4/2.0 μs	130.5	68	
Optimize morphology, crystallinity and reduce bulk defects (Cs doped into $\text{FA}_{0.75}\text{MA}_{0.25}\text{PbI}_3$)	ITO/PEDOT:PSS/MHP/PCBM/BCP/Al	—	1.15 $\times 10^{-12}$ 1.5/21 μs	—	69	
Reduce bulk defects (Cl doped into MAPbI_3)	ITO/PEDOT:PSS/MHP/PC ₆₀ /BCP/Cu	8.4×10^{-8} A cm^{-2} (-0.1 V, about 11 2.71 $\times 10^{12}$ times reduced)	—	104	70	
Optimize morphology (spray-coated CsPbBr_3 quantum dots)	FTO/TiO ₂ /MHP/Spiro-OMeTAD/Au	4×10^{-4} mA (0 V, about 20 times reduced)	1×10^{14} (365 nm)	—	90	71
Optimize morphology and crystallinity, and reduce bulk and surface defects (room-temperature crystallization for Sn-Pb MHP)	Electrode/MoO ₃ /PEDOT:PSS/MHP/PCBM/ZrAcAc/Electrode	$(2.8 \pm 0.81) \times 10^{-7}$ A cm^{-2} (0 V)	10^{11}	90 ns/2.27 μs	100	72
Optimize morphology and crystallinity (thick FAPbI_3 junctions)	ITO/Poly-TPD/Cs/MHP/C ₇₀ /BCP/Cu	—	—	60 ns (TPC extracted) ^b	—	73
Reduce bulk and surface defects (MAPbI ₃ and MAPbBr_3 thin-single-crystals)	ITO/PTAA/MHP/C ₆₀ /BCP/Cu	$1-2$ fA $\text{Hz}^{-1/2}$ (noise signal) ^a	1.5×10^{13} (532 nm)	4 ns (TPC extracted) ^b	256	74
Optimize morphology and crystallinity, and reduce bulk defects (AgI additive in $\text{CsPbI}_2\text{Br}_2$)	FTO/compact TiO ₂ /MHP/Spiro-OMeTAD/Au	9.71×10^{-6} A cm^{-2} (0 V, about 4.5 2.46 $\times 10^{11}$ times reduced)	22.4/25.7 μs	—	75	
Regulate band alignment and reduce surface defects (P3HT additive in CsSnBr_3)	ITO/ZnO/MHP/CuSCN/Ag	10^{-10} A	1.40×10^{14} (532 nm)	195.2/165.8 ms	115	76
Reduce surface defects (thioacetamide (TAA) as an interface material on CsPbBr_3)	ITO/SnO ₂ /MHP/TAA/Spiro-OMeTAD/Ag	3.13 nA cm^{-2} (0 V)	8.39 $\times 10^{-12}$	1.05/5.04 μs	118	77
Reduce surface defects and regulate band alignment (rubrene ITO/ZnO/MHP/rubrene/Au as an interface material on CsPbBr_3)	ITO/SnO ₂ /MHP/rubrene	1.04×10^{-10} A	2.61×10^{13}	79.4/207.6 μs	—	78
Reduce crystalline temperature and optimize morphology (ionic liquid 1-butyl-2,3-dimethylimidazolium chloride additive in $\text{Cs}_3\text{AgBiBr}_6$)	FTO/SnO ₂ /MHP/carbon	5 nA	1.87×10^{-12}	0.24/0.29 ms	100	79
Reduce bulk and surface defects (3-(1-pyridinio)-1-propanesulfonate (PPS) for the buried layer and the additive for MHP)	ITO/SnO ₂ /PPS/MHP:PPS/Ag	6.05×10^{-11} A (about 2 times reduced)	1.51×10^{-13}	0.74/0.09 s	—	80
Regulate band alignment and optimize crystallinity (NH_4Cl additive and DMSO solvent for $(\text{PEA})_2\text{MA}_3\text{Pb}_4\text{I}_{13}$)	ITO/PEDOT:PSS/MHP/PCBM/Bphen/Al	1.7×10^{-4} mA cm^{-2} (about 2 times 6 $\times 10^{11}$ (600 nm))	5.8/4.6 ms	126	81	
Regulate band alignment and reduce surface and bulk defects (ITO/MHP/PCBM/Ag)	—	1.31×10^{12} (570 nm)	0.532/0.521 ms	—	82	
(carboxyhydrazide (CBH) as an additive for $(\text{PEA})_2\text{MA}_3\text{Pb}_4\text{I}_{13}$)	ITO/PTAA/MHP/C ₆₀ /BCP/Cu	1.2×10^{-5} mA cm^{-2} (-0.1 V, about 5.34 $\times 10^{12}$ (850 nm))	39.68 ns (TPC extracted) ^b	224	83	
Reduce surface defects (4-amino-2,3,5,6-tetrafluorobenzoic acid (ATFB) as an additive for $\text{Cs}_{0.15}\text{FA}_{0.85}\text{Pb}_{0.5}\text{Sn}_{0.5}\text{I}_3$)	ITO/PEDOT:PSS/MHP/PCBM/Ag	10^{-8} A (-0.5 V, about 29 4.55 $\times 10^{11}$ (685 nm))	850/800 ms	—	84	
Optimize morphology and crystallinity (3,3,4,4-benzenophenonetetracarboxylic dianhydride (BPTC) as an additive for MAPbI_3)	ITO/NiO _x /MHP/PCBM/BCP/Ag	3.48×10^{-8} A cm^{-2} (-0.1 V, about 3 7.28 $\times 10^{12}$ times reduced)	5/18 μs	—	85	
Optimize crystallinity and reduce surface defects (urea as an additive for MAPbI_3)	ITO/PEDOT:PSS/MHP/Au	2.35×10^{-14} A $\text{Hz}^{-1/2}$ (noise signal) ^a	67 nGy s^{-1} (detection limit) ^b	—	86	
Reduce surface and bulk defects (trimethylolpropane triacylate (TMTA) crosslinked MAPbI_3)	ITO/SnO ₂ /MHP/Carbon	8.8 fA $\text{cm}^{-1} \text{ s}^{-1} \text{ V}^{-1}$ (drifting) ^d	4.31×10^{12}	0.06/0.26 ms	140	87
Optimize morphology and crystallinity (1-butyl-3-methylimidazolium bromide (BMIMBr) as an additive for CsPbBr_3)	ITO/PEDOT:PSS/MHP/PC ₆₁ BM/BCP/Au	2.51×10^{-10} A (0 V)	—	—	111.4	88
Regulate band alignment and optimize crystallinity (NH_4SCN and NH_4Cl as the dual additives for 2D/3D TEA-based MHP and NH_4Cl as the dual additives for 2D/3D TEA-based MHP)	ITO/PEDOT:PSS/MHP/PC ₆₁ BM/bis-C ₆₀ /Ag	1.5 pA $\text{Hz}^{-1/2}$ (noise signal) ^a	10^{12} (800–1000 nm)	7.4 μs	10^{10} (phototon number)	89
Reduce surface defects, optimize morphology and crystallinity (two-step spin-coating method for MAPbI_3)	ITO/PEDOT:PSS/MHP/PC ₆₁ BM/BCP/Au	5.55×10^{-4} mA cm^{-2} (-1.5 V, about 5 $\times 10^{11}$ (532 nm))	2.6/72.8 μs	106	90	

Table 3 (continued)

Strategy	Device structure	Dark current (density) (I_d or J_d)	D^* (Jones)	Speed [rise time (t_r)/fall (decay) time (t_f)]	LDR (dB)	Ref.
Reduce surface defects (thiophene-2-carbohydrazide (TAH), an antioxidant additive for $\text{FA}_{0.7}\text{MA}_{0.3}\text{Pb}_{0.5}\text{Sn}_{0.3}\text{I}_3$)	ITO/PEDOT:PSS/MHP/PC ₆₀ BM/ C_{60} /BCP/Ag	$1.5 \times 10^{-8} \text{ mA cm}^{-2}$ (-0.07 V)	1.8×10^{12} (840 nm) 2.5×10^{12} (940 nm)	94/97 ns	—	91
Reduce bulk and surface defects (an urea additive for MAPbI_3)	ITO/NiO _x /MHP/PCBM/BCP/Ag	$1.82 \times 10^{-11} \text{ mA cm}^{-2}$	1.42×10^{14}	—	—	92
Optimize crystallinity and reduce surface defects (tetra-fluoroborate and hexafluorophosphate additives for FAPbI_3)	ITO/PTAA/PEIE/MHP/C ₇₀ /BCP/Cu	$7.7 \times 10^{-10} \text{ A cm}^{-2}$ (-0.2 V)	10^{12}	188/630 ns	162 132	93
Optimize morphology and crystallinity, and reduce surface defects (fluorinated aminobenzoic acid isomers [3 -amino- $2,6$ -difluorobenzoic acid (13-FABA) and 4 -amino- $3,5$ -difluorobenzoic acid (14-FABA)] as additives for CsPbIBr_2)	ITO/SnO ₂ /MHP/P3HT/Ag	$2.2 \times 10^{-10} \text{ mA cm}^{-2}$ (0 V , 10^4 times reduced)	1.69×10^{13}	23.5/21.2 ms	41.93	94
Reduce bulk and surface defects (1-buty-2,3-dimethylimidazolium chloride (BMIMCl) and PMMA as additives for CsSnI_3)	ITO/SnO ₂ /MHP/Carbon	$2 \times 10^{-11} \text{ A}$	1.18×10^{12}	0.23/0.19 ms	180	95
Optimize morphology and crystallinity (Agf as an additive for CsSnI_3)	ITO/PTAA/PEIE/MHP/PC ₆₀ BM/ C_{70} /BCP/Cu	—	3.5 nGy s ⁻¹ (detection limit) ^c	280/450 ns	—	96
Optimize morphology and reduce surface defects (excess PMMA as an additive for MAPbI_3)	ITO/PEDOT:PSS/MHP/PC ₆₀ BM/Au	$3.46 \times 10^{-4} \text{ mA}$ (-1 V , about 2 times reduced)	3.38×10^{12} (532 nm)	$5.90/6.75 \mu\text{s}$	80	97
Optimize morphology and reduce bulk and surface defects (poly(ethylene glycol) (PEG) additives for CsPbI_2Br)	ITO/SnO ₂ /MHP/PTAA/MoO ₃ /Ag	$4.40 \times 10^{-8} \text{ A cm}^{-2}$ (about 778 times reduced) (-0.1 V)	1.9×10^{11} (532 nm)	0.03 ms	119	98
Optimize morphology and crystallinity, reduce surface defects (Borax) as interface materials for OMeTAD/Ag (PMMA/sodium borate salt (Borax) as interface materials for OMeTAD/Ag $\text{Cs}_{0.05}\text{FA}_{0.95}\text{MA}_{0.35}\text{Pb}(\text{BrI}_{0.6}\text{Cl}_{0.4})_3$)	ITO/SnO ₂ /MHP/Spiro-OMeTAD/Ag	$1.53 \times 10^{-9} \text{ A cm}^{-2}$ (0 V , about 8 times reduced)	7.74×10^{12} (450 nm)	$0.155/0.155 \text{ s}$	—	99
Optimize morphology and crystallinity, reduce surface defects (tin thiocyanate additive for $\text{FA}_{0.85}\text{Cs}_{0.15}\text{Sn}_{0.3}\text{Pb}_{0.5}\text{I}_3$)	ITO/PEDOT:PSS/MHP/MHP/PCBM/ZrAc/Ag	$9.85 \times 10^{-8} \text{ A cm}^{-2}$ (-0.4 V , about 60 times reduced)	8.48×10^{12} (910 nm)	$67.5 \text{ ns}/0.72 \mu\text{s}$	213	100
Optimize morphology and reduce surface defects (MAPbI_3 PMMA)	ITO/NiO _x /MHP/PCBM/ZnO/BCP/Al	$5.7 \times 10^{-7} \text{ mA}$ (0 V , about 2 times reduced)	1.07×10^{12}	$50/17 \mu\text{s}$	127	101
Reduce surface defects ($3,4,5$ -tris (<i>n</i> -decyloxy) benzoyl-amine with an azobenzene moiety (TBA-Azo) additives for Sn-BCP/Cu Pb MHP)	ITO/PTAA/MHP/TBA-Azo/PC ₆₀ /100 times reduced)	$9.61 \times 10^{-5} \text{ mA cm}^{-2}$ (-0.1 V , about 2.21 $\times 10^{11}$ (758 nm) 100 times reduced)	42.9 ns (TPC extracted) ^b	185	102	
Optimize morphology, reduce surface defects (PMMA as a double-sided passivation layer)	ITO/NiO _x /PMMA/MHP/PMMA/PCBM/ZnO/BCP/Al	$4.0 \times 10^{-7} \text{ mA cm}^{-2}$ (0 V, about 2 times reduced)	1.28×10^{12}	57/18 μs	139	103

^a Noise signal: the noise signal in photodetection is recorded by utilizing a fast Fourier transform signal analyzer combined with a preamplifier to capture the noise current at various frequencies. ^b TPC extracted: speed here can be defined as the time at which the photocurrent decays from the peak to the original $1/e$ extracted from the transient photocurrent curves. ^c Detection limit: the detection limit in X-ray detection is defined as the equivalent dose rate to produce a photocurrent greater than three times the noise current (dark current).

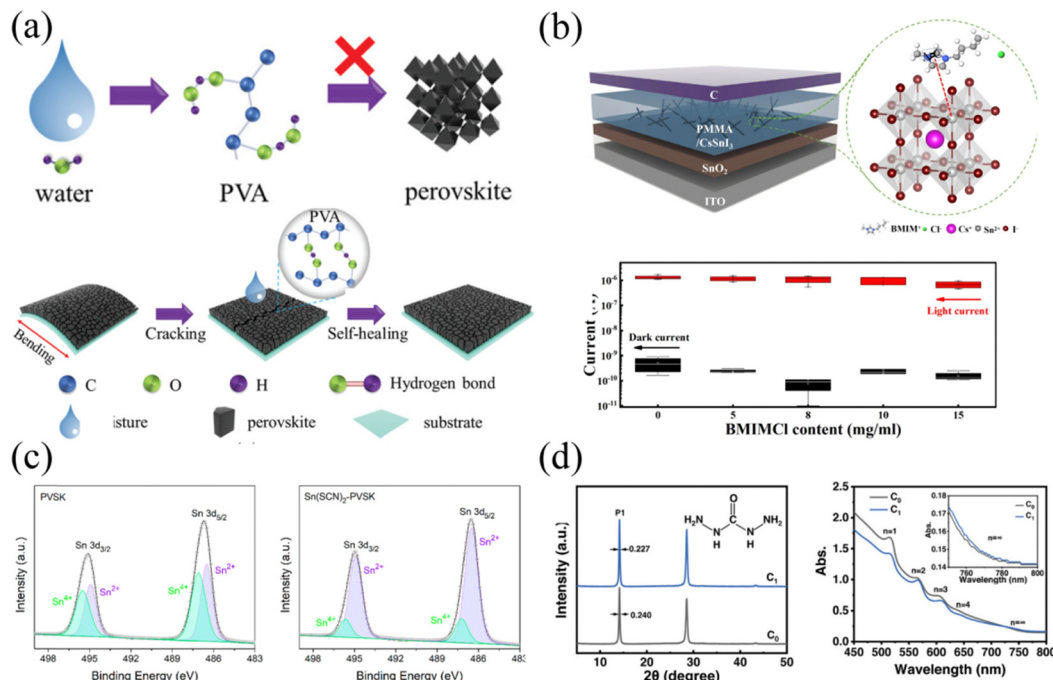


Fig. 8 (a) The mechanism of protection and self-healing process by PVA in FAPbI_3 films. Reproduced with permission.¹⁰⁴ Copyright 2021, Wiley-VCH. (b) MHPPD based on the CsSnI_3 with BMIMCl additive and photo/dark current. Reproduced with permission.⁹⁵ Copyright 2022, Nature. (c) Sn 3d XPS spectra of the pure Sn–Pb and $\text{Sn}(\text{SCN})_2$ Sn–Pb films. Reproduced with permission.¹⁰⁰ Copyright 2023, ACS. (d) XRD patterns and UV-vis absorption spectra of the control and with CBH quasi-2D MHP films. Reproduced with permission.⁸² Copyright 2023, Wiley-VCH.

carbohydrazide (CBH) additives into quasi-2D $(\text{PEA})_2\text{MA}_3\text{Pb}_4\text{I}_{13}$ precursors, resulting in significantly improved crystallinity and alignment of the 3D phase.⁸² This enhancement was evident in sharper XRD diffraction peaks and a higher ratio of the 3D MHP phase in quasi-2D MHP films, impacting their absorption characteristics (Fig. 8d).

In addition to incorporating additives in the bulk and at the interface of MHPs to passivate defects and regulate phase distribution, researchers have explored modifications to fabrication and crystallization methods to achieve the same objectives. For instance, Bao and colleagues synthesized thin single crystals of MHPs using space confinement methods to significantly reduce bulk defect density and eliminate grain boundaries in polycrystalline MHPs.⁷⁴ As depicted in Fig. 9a and b, the synthesized thin single crystals of MAPbBr_3 and MAPbI_3 exhibited excellent X-ray diffraction patterns with [100] orientation growth, and thermal admittance spectroscopy revealed a low trap state density. The resulting MHPPDs based on these thin single crystals demonstrated low noise currents of $1\text{--}2\text{ fA Hz}^{1/2}$ and ultra-low sub-pW cm^{-2} weak light detection limits. In a separate study, Zhu and colleagues introduced room-temperature crystallization in a Sn-rich binary MHP system to achieve compact and smooth Sn–Pb MHP thin films.⁷² By utilizing the strong Sn–O ionic bond between SnI_2 and dimethyl sulfoxide (DMSO), as well as the Sn–I ionic bonding between MAI and SnI_2 , the Sn-rich binary MHP precursor films could crystallize at room temperature and transform into black and smooth films after antisolvent treatment and the annealing process (Fig. 9c). These resulting thin films

were successfully demonstrated on metal–oxide–semiconductor substrates, and the MHPPDs based on this method exhibited a large LDR of 100 dB and a fast speed of $2.27\text{ }\mu\text{s}$. Wang and colleagues developed a modified two-step spin-coating method for producing large grain size and pinhole-free Pb-based MHP thin films.⁹⁰ In the modified step, MAI was intercalated with PbI_2 on the surface to form an intermediate phase, which was then transformed into the desired polycrystalline MHP film after thermal annealing (Fig. 9d). By optimizing the concentration of MAI in the MAI: PbI_2 mixture, the target thin film could be achieved (Fig. 9e). The resulting P–I–N MHPPDs based on this MHP thin film exhibited the lowest J_d of $5.55 \times 10^{-4}\text{ mA cm}^{-2}$, as well as a fast speed of $2.6\text{ }\mu\text{s}$ and $72.8\text{ }\mu\text{s}$. Furthermore, researchers have also minimized bulk defects in MHPs through the fabrication of thick MHP films using thermal evaporation methods⁷³ and the production of MHP QD films through spray-coating methods.⁷¹

5.4 Engineering of the MHP/CTL interfaces

It is important to note that shallow-energy defects can transform into deep traps in MHP films, leading to performance degradation and instability in devices. Near the surface of MHPs, the density of deep traps is significantly higher, ranging from one to two orders of magnitude greater than in the bulk. Surface defects in MHPs, including A-site, B-site, and X-site vacancies, as well as B-site antisite substitutions, are primarily responsible for the presence of surface or buried defect states. These states contribute to detrimental leakage current and the rapid degradation of MHPPDs. Moreover, the energy level

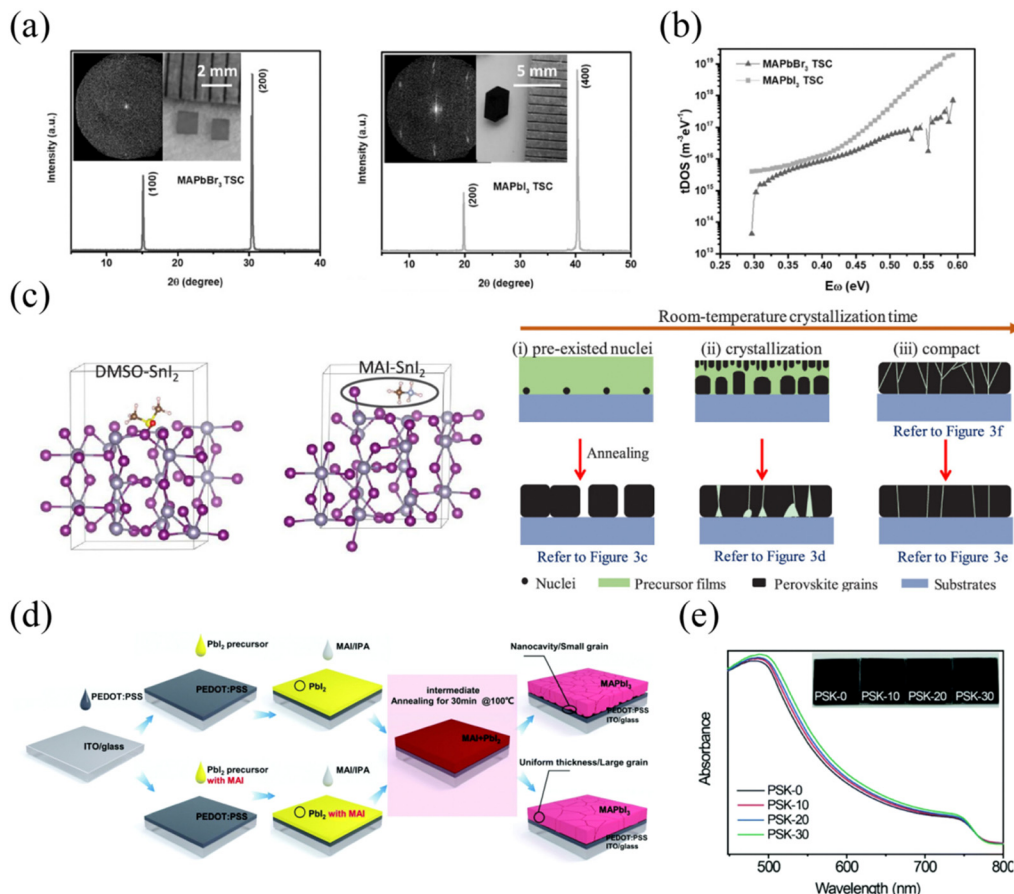


Fig. 9 (a) XRD patterns of MAPbBr₃ and b) MAPbI₃ single-crystals obtained from the 2D X-ray diffraction patterns. Insets are the 2D X-ray diffraction patterns along with the photographs of the single crystals. (b) Trap-density-of-states curves of devices based on MAPbBr₃ and MAPbI₃ single-crystals. Reproduced with permission.⁷⁴ Copyright 2017, Wiley-VCH. (c) Schematic illustrations of the bonding between SnI₂ and DMSO, and the bonding between SnI₂ and MAI, along with the crystallization process of the Sn-Pb films. Reproduced with permission.⁷² Copyright 2019, ACS. (d) Modified two-step spin-coating method for producing high-quality MAPbI₃ films. (e) Absorption curves and optical images of the various MAI concentrations are conducted in the second step. Reproduced with permission.⁹⁰ Copyright 2022, RSC.

alignment and charge extraction at the interface play a crucial role in determining the device's overall performance. Therefore, effective interface engineering between MHPs and CTLs is crucial for passivating these defects and establishing a cascade architecture, ultimately reducing J_d in MHPPDs.

The importance of interface engineering in MHPPDs differs from that in photovoltaic devices based on MHPs with a common structure involving a mesoporous oxide/MHP heterojunction or a planar architecture utilizing thin CTLs. In MHP-based photovoltaics, the large effective junction area results in a substantial parasitic capacitance, leading to slow speed and current leakage due to the presence of large crystallites in the thin film. To address this issue, Lin and colleagues achieved high-performance MHPPDs by incorporating relatively thick double fullerene hole blocking layers (HBLs) (PC₆₀BM/C₆₀). This design effectively reduced the shunt capacitance, enabling ultra-fast photo-response and suppressing current leakage by creating a large hole injection barrier.¹⁰⁵ Similarly, Fang *et al.* employed a cross-linked hole-transporting layer, *N*4,*N*4'-bis(4-(6-((3-ethyloxetan-3-yl)methoxy)hexyl)phenyl)-*N*4,*N*4-diphenylbiphenyl-4,4'-diamine (OTPD) (Fig. 10a), and controlled the thickness

of the C₆₀ layer to suppress J_d (9.1×10^{-9} A cm⁻² at -2 V) and noise current (5.5 fA Hz^{-1/2} at -0.1 V) in MHPPDs.¹⁰ In another study reported by Bao and co-workers, polyethylenimine ethoxylate (PEIE) was introduced as a substrate modifier for long-term stable inorganic MHPPDs. This modification resulted in ultra-fast MHPPDs with a speed of 602 ns to 20 ns for CsPbIBr₂ and CsPbBr₃ (Fig. 10b) over various active areas.¹⁰⁶

In addition to organic interface layers, inorganic oxide layers deposited using atomic layer deposition (ALD) show promise for suppressing J_d and enabling ultra-fast MHPPDs. Cen *et al.* utilized ALD to fabricate CsPbBr₃-based MHPPDs with Al₂O₃ and TiO₂ interfacial layers¹⁰⁷ (Fig. 10c). These layers significantly reduced current leakage by more than three orders of magnitude, leading to the successful realization of robust visible light communication systems. The investigation of organic CTLs for MHPPDs in X-ray detection has also been explored. Demchyshyn and co-workers employed PCBM and PTCDI as the HBL and PEDOT:PSS and NiO_x as the hole transport layer in a P-I-N MHPPD structure using (Cs_{0.05}(FA_{0.83}MA_{0.17})_{0.95}PbI_{3-x}Br_x) as the high energy photon absorption layer.¹⁰⁸ The results demonstrated different

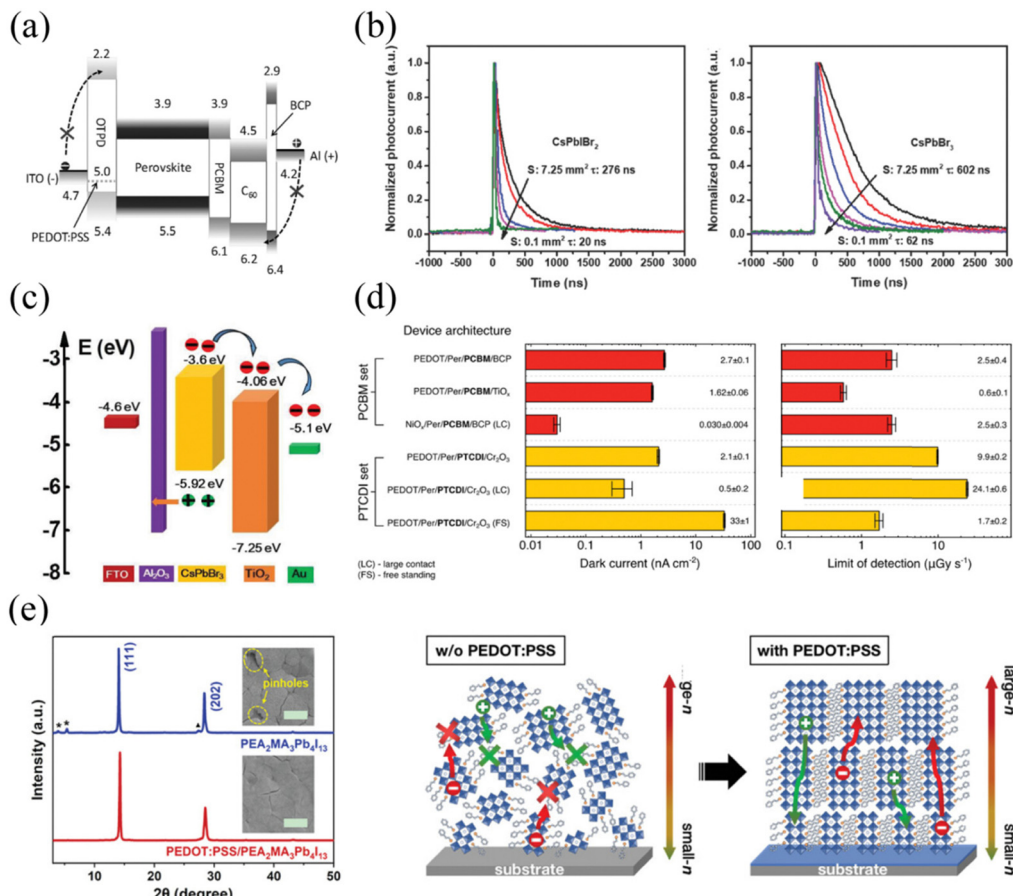


Fig. 10 (a) Energy diagram of the cross-linked OTPD MHPPDs. Reproduced with permission.¹⁰ Copyright 2015, Wiley-VCH. (b) Transient response curves of the inorganic MHPPDs with PTAA/PEIE. Reproduced with permission.¹⁰⁶ Copyright 2018, Wiley-VCH. (c) Energy band diagram of the MHPPDs with ultrathin Al₂O₃ and TiO₂ modification layers. Reproduced with permission.¹⁰⁷ Copyright 2019, Wiley-VCH. (d) Summary of the interface engineering based on several organic materials. Reproduced with permission.¹⁰⁸ Copyright 2020, Wiley-VCH. (e) XRD patterns of quasi-2D thin films without and with PEDOT:PSS interlayer (left), the insets are the corresponding top-view FESEM images (scale bar: 1 μ m), and schematic illustration of the orientational growth of MHP films without/with PEDOT:PSS interlayer. Reproduced with permission.¹⁰⁹ Copyright 2023, Wiley-VCH.

performance characteristics for different configurations, with the lowest J_d (0.030 ± 0.004 nA cm⁻²) achieved in the NiO_x/MHP/PCBM/BCP configuration and the lowest detection limit (0.58 ± 0.05 μ Gy s⁻¹) in the PEDOT/MHP/PCBM/TiO_x configuration. (Fig. 10d) Furthermore, Zhang *et al.* investigated the importance of PEDOT:PSS and PC₇₁BM in quasi-2D PEA₂MA₃Pb₄I₁₃-based MHPPDs for UV-A region detection.¹⁰⁹ The inclusion of PEDOT:PSS as the substrate enhanced the vertical orientation of PEA₂MA₃Pb₄I₁₃, as indicated by a smoother XRD pattern. (Fig. 10e) The uniform crystalline morphology and gradient phase distribution of quasi-2D MHPPDs obtained here exhibit a respectable D^* of 1.3×10^{12} Jones, along with a swift speed of 313 μ s/40.8 ms. Furthermore, extensive efforts have been directed towards introducing new CTLs and modifying both organic and inorganic CTLs to effectively passivate surface defects, construct cascades, and suppress J_d , thereby enhancing the performance of MHPPDs, as outlined in Table 4.

5.5 Heterojunctions

Forming heterojunctions with MHPs, either by using MHPs themselves or other semiconductors with superior

optoelectronic properties, offers significant advantages. These heterojunctions suppress unwanted current leakage by constructing P-N junctions and enhance device performance in several ways. They expand the photoresponse range by incorporating additional photoresponsive materials and improve stability by protecting the MHPs. Zhang *et al.* demonstrated a solution-based epitaxial method for the controlled fabrication of MHP single crystal heterojunctions, including MAPbBr₃/MAPbI₃ and MAPbCl₃/MAPbBr₃ heterojunctions.¹⁴⁸ The epitaxial growth process is illustrated in Fig. 11a. By analyzing the PL properties of different locations along the cross-section of the MHP single crystal heterojunction, the researchers confirmed the controllable gradual conversion from p-type (MAPbI₃) to n-type (MAPbBr₃) characteristics (Fig. 11b). The high-quality MHP single crystal heterojunctions with a gradient energy band structure at the heterointerface (Fig. 11b) enabled the optimized MHPPDs to achieve low detection limits for direct X-ray detection and minimal J_d drift. Likewise, Liu and colleagues employed an epitaxial method through vapor-phase deposition to establish a monocrystalline CsPbBr₃ (p-type)–SrTiO₃ (n-type) halide-oxide perovskite P-N heterojunction, as depicted in

Table 4 Summary of the engineering of the MHP/CTL interfaces for suppressing J_d and enhancing the FOMs of MHPDs

Strategy	Device structure	Dark current (density) (J_d or D^* (Jones))	Speed [rise time (t_r)/ fall (decay) time (t_f)]	LDR (dB)	Ref.
Reduce surface defects and regulate band alignment (silane barrier-capped MAPbBr ₃ quantum dots as an HBL)	ITO/PEDOT:PSS/MHP/silane barrier-capped MAPbBr ₃ quantum dot/PC ₇₁ BM/Ag	$2.19 \times 10^{-7} \text{ A cm}^{-2}$ (0 V, about 7.85 × 10 ¹² 2.5 times reduced)	—	—	110
Reduce surface defects (3,4,5-tris (<i>n</i> -dodecylxy)benzoylamide (TBA-Azo) additives for Sn-Pb MHP)	ITO/PTAA/MHP/IEICO/C ₆₀ /BCP/Cu	$9.61 \times 10^{-5} \text{ mA cm}^{-2}$ (−0.1 V, 2.21 × 10 ¹¹ about 100 times reduced) (758 nm)	42.9 ns (TPC extracted) ^b	185	102
Regulate band alignment, increase optical absorption and reduce surface defects (1,2,2'-((2Z,2')-[5,5'-(4,4,9,9-tetraakis(4-phenyl)phenyl)-4,9-dihydro-s-indacenyl]1,2-bis[5,6- <i>b</i>]-dithiophene-2,7-diy])bis[(2-ethylhexyl)oxy]thiophene-5,2-diy])bis(methanylidene))bis(3-oxo-2,3-di-hydro-1 <i>H</i> -indene-2,1-diyldiene)dimalononitrile (IEICO) as an interlayer	ITO/PTAA/MHP/IEICO/C ₆₀ /BCP/Cu	$2.6 \times 10^{-5} \text{ mA cm}^{-2}$ (−0.1 V, 1.45 × 10 ¹² about 1000 times reduced) (650 nm)	27 ns (TPC extracted) ^b	198	111
Reduce interface defects and form interfacial dipole (brominated (3-aminopropyl)triethoxysilane (APTES) as an interlayer)	Si/APTES/MHP/C ₆₀ /BCP/Au	23 nA cm ^{−2} (−1 V)	9.5 $\mu\text{Gy}_{\text{air}} \text{ s}^{-1}$ (detection limit) ^c	−/255 μs	—
Regulate band alignment and reduce interface defects ($\text{NiO}_x\text{:PbI}_2$ nanocomposites as an EBL)	ITO/NiO _x :PbI ₂ /MHP/C ₆₀ /BCP/Ag	$2 \times 10^{-10} \text{ A cm}^{-2}$ (−0.2 V)	10 ¹³	168 ns (TPC extracted) ^b	112
Regulate band alignment and reduce surface defects (MAPbI ₃ /ITO/TAPC/MHP/PBDB-T: IICIC/PC ₆ BM/Ag.	Ag.	1.01 × 10 ^{−4} mA cm ^{−2} (−0.05 V, about 4 times reduced) (600 nm)	2.17 × 10 ¹²	<400 ms	—
Regulate band alignment and increase optical absorption (FAPb _{0.5} Sn _{0.5} I ₃ /tin monosulfide quantum dots)	ITO/PEDOT:PSS/MHP/PC ₇₁ BM/BCP/Ag	$13.7 \text{ pA Hz}^{-1/2}$ (noise signal) ^c (about 2.5 times reduced) (740 nm)	2.57 × 10 ¹²	29.3/11.7 μs	106.8
Regulate band alignment and suppress electrochemical reaction (BCP as an interfacial layer between MHP and Al)	Au/Al/BCP/C ₆₀ /MHP/Au	3 nA (100 V mm ^{−1})	15 nGy _{air} s ^{−1} (detection limit) ^c	7.75/8.79 ms	—
Regulate band alignment and reduce interface defects (poly[4-(10 <i>H</i> -phenothiazin-10-yl)- <i>N,N</i> -bis(4-methoxyphenyl)aniline] (PPZ-TPA) as an EBL)	ITO/PPZ-TPA/MHP/C ₆₀ /BCP/Cu	$1.26 \times 10^{-7} \text{ A cm}^{-2}$ (−0.1 V, about 10 times reduced) (730 nm)	2.46 × 10 ¹¹	0.18 μs (TPC extracted) ^b	117
Regulate band alignment and reduce interface defects (Spiro-OMeTAD:PMMA:Cu nanocomposites as an interlayer)	ITO/SnO _x /MHP/spiro-OMeTAD/MoO ₃ /Cu	$9.72 \times 10^{-10} \text{ A cm}^{-2}$ (about 1000 times reduced)	2.7 × 10 ¹³	54.1/10.7 μs	126
Regulate band alignment and reduce interface defects (PMMA:Cu/Graphene/MoS ₂ /MHP/ZnO/Ag tandem device as an EBL)	ITO/cross-linked PVK/MHP/C ₆₀ /BCP/Cu	—	7.99 × 10 ¹⁰	0.7–0.9/0.4–0.6 μs	117
Regulate band alignment and optimize morphology (cross-linked PVK as an EBL)	ITO/PEDOT:PSS/Triazine- <i>th</i> -OMeTAD/MHP/PCBM/BCP/Cu	$5.23 \times 10^{-4} \text{ mA cm}^{-2}$ (−0.1 V, 2.06 × 10 ¹¹ about 2 times reduced) (730 nm)	0.47 ms (TPC extracted) ^b	—	121
Regulate band alignment, reduce interface defects and optimize morphology (triazine- <i>th</i> -OMeTAD as an EBL)	ITO/PCBM/BCP/Ag	1.09 nA cm ^{−2} (0 V)	8.2 × 10 ¹²	18 ns (TPC extracted) ^b	166
Optimize morphology and crystallinity, and reduce interface defects (F4-TCNQ-modified NiO _x interlayer)	ITO/NiO _x /F4-TCNQ/MHP/BCP/C ₆₀ /Cu	$1.5 \times 10^{-10} \text{ A cm}^{-2}$ (0 V, about 7.2 × 10 ¹³ 1.5 times reduced)	68.2/11.6 μs	127.1	123
Regulate band alignment and reduce interface defects (PED-OT:PSS as an EBL and the solvent optimization)	ITO/PEDOT:PSS/MHP/PC ₇₁ BM/Ag	—	1.3 × 10 ¹² (330 nm)	313 μs /40.8 ms	—
Reduce interface defects and optimize morphology (PMMA insertion between NiO _x and MHP)	ITO/NiO _x /PMMA/MHP/PCBM/ZnO/Al	From 5.9 to 5.6 × 10 ^{−8} mA cm ^{−2} (0 V)	4.5 × 10 ¹³	52/18 μs	129
Regulate band alignment (PFN as an HBL)	ITO/PEDOT:PSS/MHP/PCBM/PFN/Al	<1 pA Hz ^{−1/2} (noise signal) ^a	4 × 10 ¹⁴	180/160 ns	>100

Table 4 (continued)

Strategy	Device structure	Dark current (density) (I_d or J_d)	D^* (Jones)	Speed [rise time (t_r)/ fall (decay) time (t_d)] (dB)	LDR	Ref.
Reduce interface defects and optimize crystallinity (Mg doped ITO/Mg-doped NiO/MHP/C ₆₀ /BCP/Cu NiO as an EBL)	ITO/CuInSe ₂ quantum dots: PEDOT:PSS/ MHP/PCBM/Ag	$2.2 \times 10^{-9} \text{ A cm}^{-2}$ (−0.1 V, about 3 times reduced)	5.3×10^{13} (640 nm) 115.32/11.30 μs	1.02 × 10 ¹³ (580 nm)	124	126
Regulate band alignment, reduce interface defects and increase optical absorption (CuInSe ₂ quantum dots: PED-OT:PSS as a hybrid EBL)	ITO/NiO _x /MHP/PCBM/ZnO/BCP/Al	$7.84 \times 10^{-6} \text{ mA cm}^{-2}$ (0 V, about 4 times reduced)	3.6×10^{11}	<0.02 s	—	132
Regulate band alignment and optimize crystallinity (NiO _x as ITO/NiO _x /MHP/PCBM/ZnO/BCP/Al an EBL)	ITO/PEDOT:PSS/PTAA/MHP/PCBM/Phen-NaDPO/Ag	$2.3 \times 10^{-27} \text{ A}^2 \text{ Hz}^{-1}$ (noise signal) ^a	2.3×10^{13} (660 nm) 2.89/1.93 μs	—	—	128
Regulate band alignment and optimize crystallinity (PED-OT:PSS/PTAA as a double-EBL)	ITO/PEDOT:PSS/Nafton/MHP/PCBM/Al	—	—	—	—	127
Optimize morphology and crystallinity (PEIE modified PTAA substrate)	ITO/PTAA/PEIE/MHP/PCBM/BCP/Ag	$6.0 \times 10^{-6} \text{ mA cm}^{-2}$ (−0.3 V, about 600 times reduced)	$1.57/15.5 \mu\text{s}$	2.54 × 10 ¹¹ (395 nm)	156	129
Regulate band alignment (introduction of TiO ₂ and Spiro-OMeTAD as interfacial layers)	FTO/TiO ₂ /MHP/spiro-OMeTAD/Au	$<10^{-13} \text{ A Hz}^{-1/2}$ (noise signal) ^a	9.7×10^{12} (525 nm) 20 ns (TPC extracted) ^b	460/556 ns	200	106
Regulate band alignment and reduce interface defects (PVP modified SnO ₂ as an EBL)	ITO/SnO ₂ /PVP/MHP/Spiro-OMeTAD/Au	$1.8 \times 10^{-8} \text{ mA cm}^{-2}$ (−0.05 V, about 10 times reduced)	1.13×10^{13}	—	130	130
Regulate band alignment, reduce interface defects and optimize morphology (ALD TiO ₂ /Spin-coated TiO ₂ as HBLs)	FTO/Bi-TiO ₂ /MHP/Ag	$10^{-10} \text{ A (0 V, about 100 times 10}^{12}$ reduced)	$6.8/5.5 \mu\text{s}$	—	132	131
Regulate band alignment and promote band bending (P3HT-COOH as an EBL)	FTO/P3HT-COOH/MHP/PCBM/PEI/Ag	$0.042 \times 10^{-6} \text{ A cm}^{-2}$ (−0.1 V, about 38 times reduced)	9.5 ns	—	80	132
Regulate band alignment (PEDOT:PSS or NiO _x /MHP/PCBM or PCBM or PTCDI as an HBL)	ITO/PEDOT:PSS or NiO _x /MHP/PCBM or PTCDI/TiO ₂ /Al	$0.030 \pm 0.004 \text{ nA cm}^{-2}$	$0.58 \pm 0.05 \mu\text{Gy s}^{-1}$ (detection limit) ^c	—	—	135.2
Regulate band alignment (TiN as a blocking layer between MHP and electrode)	ITO/PTAA/PVP/MHP/PCBM/C ₆₀ /TiN/Ag	$3.25 \times 10^{-11} \text{ A cm}^{-2}$ (−0.5 V)	1.21×10^{14} (720 nm)	105.7/106.7 μs	164	135
Regulate band alignment (PCBM:PMMA as an HBL)	ITO/PEDOT:PSS/MHP/PCBM:PMMA/Al	$2.3 \times 10^{-6} \text{ mA cm}^{-2}$ (−0.01 V, about 65 times reduced)	1.1×10^{13} (532 nm) 3.0/2.2 μs	—	112	136
Optimize morphology and crystallinity, and regulate band alignment (Al ₂ O ₃ and TiO ₂ as interfacial modification layers)	FTO/Al ₂ O ₃ /MHP/TiO ₂ /Au	$10^{-11} \text{ A (about 1000 times reduced)}$	1.88×10^{13} (405 nm)	28/270 μs	—	172.7
Regulate band alignment and reduce interface defects (rGO:TS-CuPc nanocomposites as the interfacial layer)	ITO/rGO:TS-CuPc/MHP/PCBM/BCP/Ag	$2.2 \times 10^{-8} \text{ A cm}^{-2}$ (−0.1 V, about 10 times reduced)	4.2×10^{12}	<47/47 ms	118	137
Regulate band alignment, optimize morphology and reduce interface defects (NiO _x and TiO ₂ as interfacial layers)	ITO/NiO _x /MHP/TiO ₂ /Au	$10^{-11} \text{ A (about 10}^4 \text{ times reduced)}$	1.59×10^{13}	0.056/0.25 ms	—	186.7
Regulate band alignment and reduce surface defects (OTPD/BCP/PCBM/C ₆₀ /BCP/Al as an EBL and PCBM/C ₆₀ as HBLs)	ITO/OTPD/MHP/PCBM/C ₆₀ /BCP/Al	$9.1 \times 10^{-9} \text{ A cm}^{-2}$ (−2 V, about 50 times reduced)	7.4×10^{12} (680 nm) 0.12 μs (TPC extracted) ^b	—	94	10
Regulate band alignment (NiO _x as an EBL)	ITO/PEDOT:PSS or NiO _x /MHP/C ₆₀ /BCP/Au	—	$12 \mu\text{Gy s}^{-1}$ (detection limit) ^c	248/— ms	—	139
Regulate band alignment and reduce interface defects (TiO ₂ as an HBL)	PCBM as HBLs)	—	3.39×10^{11} (405 nm)	500 ns (estimated)	100	140
Optimize morphology, regulate band alignment and reduce interface defects (TiO ₂ as an HBL)	ITO/TiO ₂ /PC ₆ 1BM/MHP/P3HT/MoO ₃ /Ag	—	1.8×10^{12} (640 nm) —	—	86	142
Reduce surface defects and regulate band alignment (P3HT as an EBL)	ITO/PEDOT:PSS/MHP/PCBM/C ₆₀ /LiF/Au	$5 \times 10^{-10} \text{ A cm}^{-2}$ (−0.5 V)	10^{12}	1.7/1.0 μs	230	105
Regulate band alignment (PCBM/C ₆₀ as HBLs)	ITO/PTAA/Al ₂ O ₃ /MHP/PMMA/PCBM/BCP/	$1.5 \times 10^{-14} \text{ A Hz}^{-1/2}$ (noise signal) ^a	5.4×10^{12} (532 nm) 597 ns (TPC extracted) ^b	—	160	143
Reduce interface defects and optimize morphology and crystallinity (Al ₂ O ₃ as a bottom interlayer and PMMA as a surface Ag interlayer)	FTO/TiO ₂ , Al ₂ O ₃ , PCB as HBLs)	—	—	—	31	31
Regulate band alignment (TiO ₂ , Al ₂ O ₃ , PCB as HBLs)	FTO/Ag _x Ag _{1-x} /Al ₂ O ₃ , PCB as HBLs)	$0.012 \pm 0.005 \mu\text{A cm}^{-2}$	$(6.0 \pm 1.3) \times 10^{12}$	1.2/3.2 μs	—	113
Reduce interface defects (Li doped VO _x as an EBL)	FTO/Li doped VO _x /MHP/PCBM/BCP/Ag	1.23×10^{13}	—	—	113	144

Table 4 (continued)

Strategy	Device structure	Dark current (density) (J_d or J_d)	D^* (Jones)	Speed [rise time (t_r)/ fall (decay) time (t_d)]	LDR (dB)	Ref.
Reduce surface defects (PCBM and aluminum doped ZnO as ITO/PEDOT:PSS/MHPP/PCBM/AZO/Al HBLs)	ITO/PEDOT:PSS/MHPP/PC ₆₀ BM or PC ₇₀ BM/BCP/Ag	$3.38 \times 10^{-9} \text{ A cm}^{-2}$ (-0.1 V , about 270 times reduced) $1.4 \times 10^{-7} \text{ A cm}^{-2}$ (-1 V)	—	0.29 μs (TPC extracted) ^b 100 ns (TPC extracted) ^b	57	145
Optimize morphology (PC ₆₀ BM or PC ₇₀ BM as HBLs)	ITO/NiO _x /MHPP/SnO ₂ /Au	33.41 fA $\text{Hz}^{-1/2}$ (noise signal) ^a	2.05×10^{12}	150.2/159.7 ns	>90	146
Reduce surface defects ($\text{Cs}_{0.1}\text{MA}_{0.3}\text{FA}_{0.6}$)AgBi ₆ as an interface ITO/NiO _x /MHPP/SnO ₂ /Au layer for $\text{Cs}_{0.05}\text{MA}_{0.65}\text{FA}_{0.3}\text{PbI}_3$		17.5 pA cm^{-2}	0.43 $\mu\text{Gy s}^{-1}$ (detection limit) ^c	0.2/0.5 s	—	147

^a Noise signal; the noise signal in photodetection is recorded by utilizing a fast Fourier transform signal analyzer combined with a preamplifier to capture the noise current at various frequencies. ^b TPC extracted: speed here can be defined as the time at which the photocurrent decays from the peak to the original $1/e$ extracted from the transient photocurrent curves. ^c Detection limit: the detection limit in X-ray detection is defined as the equivalent dose rate to produce a photocurrent greater than three times the noise current (dark current).

Fig. 11c.¹⁴⁹ The inclusion of rigid SrTiO_3 not only increased device stability by preventing anion interdiffusion between CsPbBr_3 and SrTiO_3 , leading to an effective operating temperature of 150 °C for the MHPPD, but also facilitated the formation of a sharp P–N interface with CsPbBr_3 , ensuring low J_d and satisfactory photoresponse. Furthermore, Wang *et al.* demonstrated a P–I–N heterojunction (n-type, Bi-doped MAPbBr_3)/(intrinsic, $\text{MAPbBr}_{2.5}\text{Cl}_{0.5}$)/(p-type, Ag-doped MAPbBr_3) by a solution-processed dopant incorporated epitaxial growth method.¹⁵⁰ To identify suitable dopants, researchers investigated the thermal-probe-induced effects of MHPs incorporating different dopants. After optimization, 0.1 M AgBr-doped and 0.2 M Bi-doped MAPbBr_3 were grown on opposite faces of the $\text{MAPbBr}_{2.5}\text{Cl}_{0.5}$ substrate to form a P–I–N heterojunction (Fig. 11d). Benefiting from the efficient P–I–N junction, which provides sufficient charge barriers and facilitates energy alignment, the MHPPDs exhibited a low J_d of 11 nA cm^{-2} under 500 V cm^{-1} and a lowest detection limit of 16 nGy s^{-1} . More recently, Zou and colleagues developed a dual-band heterojunction configuration of $\text{MAPbBr}_3/\text{PCBM}/\text{FASn}_{0.5}\text{Pb}_{0.5}\text{I}_3$ using a high-throughput blading method for ultra-fast MHz imaging and communication speeds (Fig. 11e).¹⁵¹ This dual-band heterojunction, benefiting from the absorption of both wide (MAPbBr_3) and narrow ($\text{FASn}_{0.5}\text{Pb}_{0.5}\text{I}_3$) MHPs and tuning of the polarity and amplitude of the bias voltage, enabled MHPPDs based on this structure to achieve a D^* of $1.25/3.10 \times 10^{12}$ Jones and bandwidths of 16.5/>20 MHz for the visible/NIR bands.

Additionally, researchers have developed MHP heterojunctions incorporating narrow band gap ionic dyes (Fig. 12a) and QDs (Fig. 12b) to extend light absorption deep into NIR regimes and effectively suppress device J_d through precise gradient energy alignment design.^{152,153} For the UV regime of the heterojunction in MHPPDs, Ga_2O_3 (Fig. 12c) and ZnO (Fig. 12d) were employed to achieve efficient carrier separation and broaden the photoresponse of MHPPDs.^{154,155} Table 5 compares the performance parameters of recent MHPPDs based on various heterojunctions.

5.6 Architecture modification

The device architecture plays a crucial role in reducing J_d and enhancing the FOMs of MHPPDs. By controlling the stacking type of materials, manipulating the electrodes, and incorporating extra devices into the MHPPDs, it is possible to efficiently mitigate J_d and increase the FOMs of MHPPDs. For example, Song *et al.* designed lateral P–I–N single crystal MHPPDs to isolate the electrodes from contacting the MHP surface, in contrast to conventional metal–semiconductor–metal photodiodes, as illustrated in Fig. 13a.¹⁸⁰ The resulting devices exhibited nearly three orders of magnitude suppression of J_d compared to the metal–semiconductor–metal devices. Moreover, they demonstrated environmental stability by avoiding the interfacial electrochemical reaction between the electrode and MHP. In another approach, Jin *et al.* developed a MHPPD architecture by adding a shunting electrode as a blanking unit to suppress J_d .¹⁸¹ As depicted in Fig. 13b, electrons are emitted

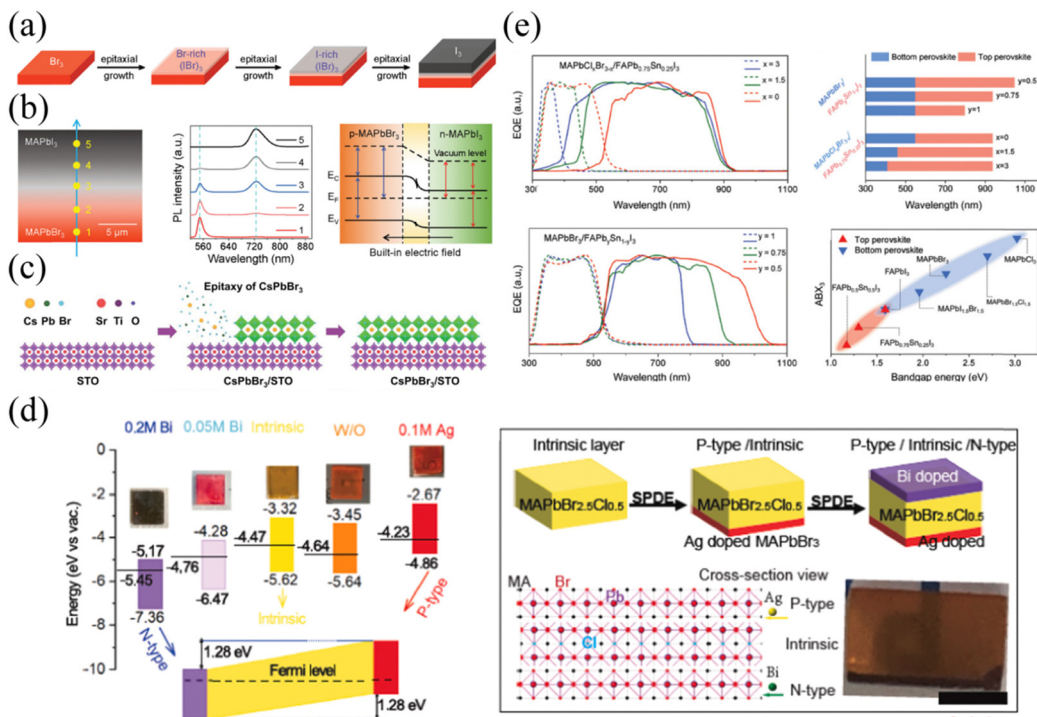


Fig. 11 (a) Epitaxial growth process of the MHP heterojunction. (b) Positions for PL measurements (left), PL spectra (middle), and band diagram of the MHP heterojunction without bias (right). Reproduced with permission.¹⁴⁸ Copyright 2023, Wiley-VCH. (c) Schematic diagram of the vapor-phase epitaxy of the CsPbBr_3 thin film on halide–oxide perovskite. Reproduced with permission.¹⁴⁹ Copyright 2023, Wiley-VCH. (d) Energy diagram and the fabrication process of the MHP heterojunction by doping in the epitaxial growth. Reproduced with permission.¹⁵⁰ Copyright 2021, Elsevier. (e) Optoelectronic properties of the double MHP heterojunction thin films. Reproduced with permission.¹⁵¹ Copyright 2024, Wiley-VCH.

from the source to the drain electrode with two lateral terminals in the dark. To minimize the absolute value of J_{d} , a top dark-current-shunting electrode on the MHP films was utilized to attract the emitted electrons, leading to effective shunting of mobile electrons under dark conditions. This design resulted in an ultra-low J_{d} of 51.1 pA cm^{-2} and a detection limit of 7.84 nGy s^{-1} . Additionally, Zhan *et al.* introduced a modification to the device structure by presenting a MHPPDs crossbar array through vapor deposition.¹⁸² This array consisted of a P-I-N diode (ITO/PEDOT:PSS/MHP/PCBM/BCP) and a reverse blocking diode (PCBM/BCP/ PbI_2 /Spiro-TTB) in a vertically stacking sequence, with PCBM/BCP serving as the co-cathode, as shown in Fig. 13c. The presence of the blocking diode established an efficient barrier to prevent electron transfer to the Ag electrode. This configuration is fully scalable and compatible with integrated circuits, making it suitable for the industrialization of image sensors. The devices and the corresponding strategies for architecture modification and performance parameters are summarized in Table 6.

6. Summary and perspectives

Due to their remarkable optical and electrical properties, MHPPDs have showcased unparalleled performance, surpassing commercially available inorganic counterparts in recent years. In addition, formidable progress has been made in developing robust optoelectronic applications such as static

imaging for visible and X-ray spectra,^{141,186} real-time dynamic imaging,¹⁸² communications,^{102,107} and health monitoring.^{91,187} Despite this, MHPPDs still face challenges related to defects within their structure that impair the dynamics of charge carriers, diminishing photodetection performance metrics like J_{d} , LDR, D^* , and speed. To address these issues, a deep understanding of J_{d} 's origin in MHPPDs is critical. Research has been directed towards component and dimensional engineering to mitigate defects within the bulk and interfaces, interfacial engineering, the integration of heterojunctions, and adjustments to device architectures. Tables 1–6 encapsulate the enhancements in J_{d} and other FOMs demonstrated using these strategies. Future research targeting superior performance and durability in optoelectronic devices, facilitating detection across a broad spectral range from ionizing radiation to near-infrared, is indispensable. Achieving high EQE or R while simultaneously suppressing the J_{d} in MHPPDs is critical and challenging. Both EQE (or R) and J_{d} are highly dependent on carrier generation, extraction, and recombination processes. The efficiency of these processes directly impacts EQE (or R) and J_{d} . For instance, the quality of the MHP films and the interfaces between the MHP and the EBL as well as the HBL are essential for influencing charge transportation and recombination, thereby impacting EQE (or R) and J_{d} . The mobility and stability of the EBL and HBL are highly relevant to charge extraction and recombination at the interface between MHP and EBL/HBL, thereby also affecting EQE (or R)

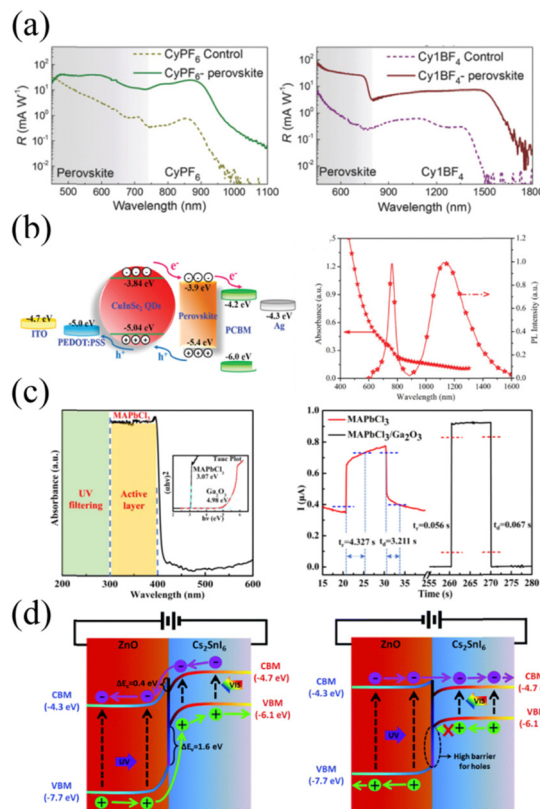


Fig. 12 (a) Photoresponse of the CyPF₆, Cy₁BF₄, and MHP-CyPF₆, Cy₁BF₄ heterojunction MHPPDs. Reproduced with permission.¹⁵² Copyright 2017, Wiley-VCH. (b) Energy band diagram of the MHP/CulnSe₂ QDs heterojunction (left), the absorption and PL spectra of the MHP/CulnSe₂ QD thin film (right). Reproduced with permission.¹⁵⁶ Copyright 2020, Wiley-VCH. (c) Absorption spectrum and bandgap of MAPbCl₃ and amorphous Ga₂O₃ films (left), the $I-t$ curves of the MAPbCl₃/amorphous Ga₂O₃-based devices (right). Reproduced with permission.¹⁵⁷ Copyright 2022, Elsevier. (d) Energy band diagram showing the band alignment and carrier dynamics of the CsSnI₆/ZnO device under different biases. Reproduced with permission.¹⁵⁵ Copyright 2020, RSC.

and J_d . Furthermore, mechanical stress at the interface between MHP and EBL/HBL can introduce defects that deteriorate EQE (or R) and J_d . Therefore, by employing advanced passivation techniques, improved fabrication methods, and optimized device architectures aimed at increasing the quality of the MHP film, EBL/HBL, and the interface between MHP and EBL/HBL, it is possible to develop MHPPDs with high EQE (or R) and low J_d .

Central to advancing MHPPDs is an in-depth understanding of the origins of J_d . Current research predominantly employs the conventional semiconductor-based photodiode model grounded in thermodynamics. However, given MHPs' ionic characteristics, it is pivotal to develop a nuanced MHPPD model accounting for ion migration within the bulk and interfaces—an imperative for light sensing and direct radiation detection applications. A comprehensive model must also incorporate interactions between MHPs, CTls, and electrodes to thoroughly describe charge carrier behavior under dark conditions.

Addressing the defects present in MHPs is the crucial strategy for substantially reducing the J_d in MHPPDs. These defects, located in the bulk and at the interfaces of MHPs, are recognized as major contributors to elevated J_d levels and undesirable periods of J_d drift in MHPPDs. Thankfully, numerous effective strategies have emerged which include component, additive, and interfacial engineering. Among these, strategic component selection is particularly promising in mitigating issues such as ion migration and phase transitions caused by these defects. Monovalent cations like FA are highly competitive in MHPs used in MHPPDs for broadband light detection, owing to their lower bandgap and improved thermal and light stability compared to other cations. Similarly, the choice of halide ions plays a critical role. Beyond just tuning the absorption spectrum of the devices, previous studies have highlighted the beneficial effects of various halide anions on the crystallization process and defect suppression in MHP films. Notably, Cl⁻ and bromine Br⁻ ions, at certain concentrations, can enhance crystallinity, morphology, and stability of MHPs, which in turn boosts photodetection performance.

Passivation techniques involving additives in MHP precursor solutions and interfacial engineering are critical for defect suppression and overall device performance enhancement. It is imperative to develop thoughtful additive design strategies and more resilient CTls that consider the multifunctional effects of additives and the complexities of surface defect configurations. Moreover, there is a need for continued research into strategies for constructing heterojunctions either with MHPs or with other superior optoelectronic materials. These heterojunctions could help in managing surface defects, aligning energy bands, and improving optoelectronic properties, thus potentially mitigating J_d and minimizing periods of J_d drift in MHPPDs.

Further rethinking of the architecture of MHPPDs can serve to effectively suppress J_d . Introducing additional layers, such as EBL or HBL, can prevent charge carriers from being injected from the electrodes into the MHP, thereby reducing J_d . The alignment of material energy levels, as well as both vertical and lateral architectural designs, are crucial in influencing the charge dynamics within the device. Additionally, the implementation of electrical regulation methods can effectively curb J_d and further diminish J_d drift periods.^{181,188} Future research should focus on simplifying device structures and developing strategies suitable for large-scale industrial production.

Controlling the operational temperature of MHPPDs has shown potential in minimizing J_d and enhancing device performance. Lower temperatures effectively restrain thermal excitation of charge carriers, thereby reducing J_{diff} generation. This temperature-dependent suppression offers promising prospects for achieving enhanced D^* in MHPPDs. Moreover, operating at cooler temperatures can increase the stability and lifespan of MHP films by curbing degradation processes. However, maintaining an optimal temperature is essential; excessively low temperatures may impair the device's response time and sensitivity. Therefore, it is critical to finely tune the

Table 5 Summary of the heterojunctions with MHP for suppressing J_d and enhancing the FOMs of MHPDs

Strategy	Device structure	Dark current (density) (J_d or J_d)	D^* (Jones)	Speed [rise time (t_r)/fall (decay time t_f)]	LDR (dB)	Ref.
Generate injection barrier and reduce interface defects (MAPbBr ₃ /Bi ³⁺ -doped MAPbCl ₃ single crystals)	Au/MAPbBr ₃ /Bi ³⁺ -doped MAPbCl ₃ /Au	0.78 nA (-100 V)	—	4.89 μ s (TPC extracted) ^b	—	159
Establish the built-in electrical field (electrochemical-deposition NiO _x /Cs _x Bi ₂ Br ₉)	FTO/NiO _x /MHP/Ag	1.3 \times 10 ⁻¹² A Hz ^{-1/2} (noise signal) ^a	1.3 \times 10 ¹¹	3.04/4.66 ms	116.6	160
Establish the built-in electrical field (Cs ₃ PbBr ₆)	FTO/SnO ₂ /CsPbBr ₃ /Cs ₃ PbBr ₆ /P3HT:PCBM/Au	63 nA cm ⁻² (4 V, about 1.3 times reduced)	15 nGy ⁻¹ (detection limit) ^c	1.6/1.2 ms	—	156
Regulate band alignment (GaN/CS ₂ AgBiBr ₆ /NiO)	In/GaN/MHP/NiO/Au	1.89 \times 10 ⁻⁹ A (0 V)	3.28 \times 10 ¹¹ (365 nm)	151/215 μ s	—	157
Establish the built-in electrical field (MAPbCl ₃ /Bi ³⁺ -Ag/ MAPbCl ₃ /Bi ³⁺ -doped MAPbCl ₃ single crystals)	Ag/MAPbCl ₃ /Bi ³⁺ -doped MAPbCl ₃ /single crystals/Au	2.15 μ A cm ⁻² (-20 V)	4.87 \times 10 ¹¹ (393 nm)	176.3 ns/11.6 μ s	—	158
Establish the built-in electrical field (PVP-modified MAPbCl ₃ single crystals)	—	—	1.5 \times 10 ⁻¹² (405 nm)	645/560 μ s	44	161
Establish the built-in electrical field (planar-type MAPhCl ₃ -x _x Si)	Pt/Ag ⁺ -doped MAPbBr ₃ /Sb ³⁺ -doped MAPbBr ₃ /Au/Poly-TPD/MAPbBr _{2.5} Cl _{0.5} /MAPbCl ₃ /Ag	300 fA Hz ^{-1/2} (0 V)	6.39 \times 10 ¹¹ (530 nm)	14/10 ms	—	162
Establish the built-in electrical field (planar-type Ag ⁺ -doped MAPbBr ₃ /Sb ³⁺ -doped MAPbBr ₃)	1.12 \times 10 ⁻¹⁰ A Hz ^{-1/2} (noise signal) ^a	7.32 \times 10 ⁷ (500 nm)	10/15 μ s	—	163	
Establish the built-in electrical field (MAPbBr _{2.5} Cl _{0.5} /MAPbCl ₃)	(-100 V) 0.15 pA Hz ^{-1/2}	5.88 \times 10 ¹¹ (378 nm)	4.3/5.2 μ s	119	155	
Establish the built-in electrical field (ZnO/CS ₂ SnI ₆)	ITO/ZnO/MHP/Au	0.13 nA	2.23 \times 10 ¹² (815 nm)	13.0/14.6 ms	—	164
Establish the built-in electrical field (Si/SnO ₂ /MAPbI ₃ /MoO ₃ /Ag)	Al/Si/SnO ₂ /MAPbI ₃ /MoO ₃ /Ag	5.46 fA Hz ^{-1/2} (about 20% reduced)	6.07 \times 10 ¹¹ (390 nm)	28/— μ s	—	165
Establish the built-in electrical field (ZnO/PTAA/ MAPbCl ₃)	ITO/ZnO/MHP/PTAA/MoO _x /Ag	—	—	—	—	—
Reduce interface defects and regulate band alignment (2D/3D MHP/O6T-4F)	ITO/PLAA/MHP/O6T-4F/C ₆₀ /BCP/Al	3.57 \times 10 ⁻¹⁰ mA cm ⁻² (-0.5 V, about 1.06 \times 10 ¹⁵ (500 nm) 8 times reduced)	2.9/4.8 μ s	110	166	
Establish the built-in electrical field (MAPbI ₃ /TiO ₂)	FTO/TiO ₂ /MHP/Spiro-OMeTAD/Au	-5 nA (0 V)	7.8 \times 10 ⁻¹⁰ (494 nm)	—	—	167
Establish the built-in electrical field ((BA) ₂ (MA)Pb ₂ I ₇ /(BA) ₂ MA ₂ Pb ₂ I ₇)	FTO/MHP/Cr/Au	10 ⁻⁶ A cm ⁻² (about 10 ³ times reduced)	—	150/170 ms	—	168
Establish the built-in electrical field and increase optical absorption (NiO/MAPbI ₃)	FTO/PEDOT:PSI/CuInSe ₂ quantum dots/MHP/PCBM/Ag	—	10 ¹⁰	320 \pm 10/305 \pm 10 ms	—	169
Regulate band alignment and increase optical absorption (CuInSe ₂ quantum dots/MAPbI ₃)	FTO/PEDOT:PSI/CuInSe ₂ quantum dots/MHP/PCBM/Ag	8.7 fA Hz ^{-1/2} (noise signal) ^a	7.0 \times 10 ¹⁰ (580 nm)	277 ns (TPC extracted) ^b	75.16	153
Establish the built-in electrical field and impede the anion interdiffusion (CsPbBr ₃ /SrTiO ₃)	Au/CsPbBr ₃ /SrTiO ₃ /Ag	2.01 \times 10 ⁻¹² A (-1 V)	7.7 \times 10 ¹¹ (850 nm)	2.06/0.30 s	—	149
Establish the built-in electrical field (SnO ₂ /Cs ₂ AgBiBr ₆)	FTO/SnO ₂ /MHP/Au	2 nA (about 280 times reduced)	2.1 \times 10 ¹²	248/341 μ s	108	170
Reduce interface defects and increase optical absorption (MAPbI ₃ /PDPPTDTPr:PCBM)	ITO/PTAA/MHP/PDPPTDTPr:PCBM/Cu	8.7 \times 10 ⁻⁵ mA cm ⁻² (-0.3 V, about 100 times reduced)	1 \times 10 ¹¹ (900 nm)	5 ns (TPC extracted) ^b	95	171
Establish the built-in electrical field (MAPbI ₃ /PTB7/C ₆₀)	ITO/PEDOT:PSI/MHP/PTB7/C ₆₀ /BCP/Ag	1.85 \times 10 ⁻⁵ mA cm ⁻² (-0.1 V)	1.37 \times 10 ¹² (680 nm)	3.9/4 μ s	141	172
Establish the built-in electrical field (MAPbBr ₃ -nCl _n /CsPbBr ₃)	Au/MAPbBr ₃ -nCl _n /CsPbBr ₃ /Au	0.5 μ A cm ⁻²	96 nGy s ⁻¹ (detection limit) ^c	—	—	173
Establish the built-in electrical field (MAPbBr ₃ single crystal)	Au/MAPbCl ₃ /MAPbBr ₃ /Au	3.92 \times 10 ⁻⁴ nA cm ⁻¹ s ⁻¹ V ⁻¹ (drifting) ^d	7 \times 10 ¹¹	0.43/1.39 s	—	174
Establish the built-in electrical field (Bi-doped MAPbBr ₃ /MAPbBr _{2.5} Cl _{0.5} /Ag-doped MAPbBr ₃)	Au/Bi-doped MAPbBr ₃ /MAPbBr _{2.5} Cl _{0.5} /Ag-doped MAPbBr ₃ /Au	11 nA cm ⁻² (-0.07 V)	16 nGy s ⁻¹ (detection limit) ^c	-750 ns	—	150

Table 5 (continued)

Strategy	Device structure	Dark current (density) (I_d or J_d)	D^* (Jones)	Speed [rise time (t_r)/fall (decay) time (t_f)]	LDR (dB)	Ref.
Establish the built-in electrical field and regulate band alignment (MAPbCl ₃ /MAPbBr ₃ single crystal)	Au/MAPbCl ₃ /MAPbBr ₃ /Au	—	12.2 nGy s ⁻¹ (detection limit) ^c	1.5/1.6 ms	—	148
Establish the built-in electrical field ($\text{Cs}_2\text{AgBiBr}_6$ / $(\text{C}_{3.8}\text{H}_{34}\text{P}_2)\text{MnBr}_4$)	Au/Cs ₂ AgBiBr ₆ / $(\text{C}_{3.8}\text{H}_{34}\text{P}_2)\text{MnBr}_4$ /C ₆₀ /BCP/Cr	20 pA Hz ^{-1/2} (noise signal) ^a	0.2 μGy (detection limit) ^c	41 ns (TPC extracted) ^b	—	175
Regulate band alignment and establish the built-in electrical field ($\text{Cs}_{0.15}\text{FA}_{0.85}\text{Pb}(\text{I}_{0.15}\text{Br}_{0.85})_3/\text{Cs}_{0.15}\text{FA}_{0.85}\text{PbI}_3$)	Carbon/Cs _{0.15} FA _{0.85} Pb(I _{0.15} Br _{0.85}) ₃ /BCP/Cr	5.3×10^{-7} nA cm ⁻¹ s ⁻¹ (drifting) ^d	(1000 V mm ⁻¹) s ⁻¹	6.1 μs	—	176
Establish the built-in electrical field (MAPbI ₃ / $\text{PDPP3T:PC}_{71}\text{BM}$)	ITO/PEDOT:PSS/MHPH/PDPP3T:PC ₇₁ BM/Al	3.6×10^{-9} A cm ⁻² (−0.1 V, about 5 times reduced)	3×10^{13}	4.82/4.30 μs	112	177
Establish the built-in electrical field and increase optical absorption (MAPbI ₃ /graphene quantum dots/Porous Si)	InGa/BCP/Si/P-Si/MHPH/Au	—	7.6×10^{10}	654/735 ns	80	178
Establish the built-in electrical field and increase optical absorption (MAPbCl ₃ /amorphous Ga ₂ O ₃)	FTO/Ga ₂ O ₃ /MHP/Spiro-OMeTAD/Ag	1.042 nA (about 330 times reduced)	5.4×10^{10}	56/67 ms	80	154
Establish the built-in electrical field and increase optical absorption (MAPbBr ₃ /FASh _{0.5} Sh _{0.5} I ₃)	FTO/PEDOT:PSI/MHP/PCBM/MHP/P3HT:Ag	1.3×10^{-10} mA cm ⁻² (−0.5 V, 7000 times reduced)	1.25×10^{12}	124.5/37.2 ns	102	151
Establish the built-in electrical field and increase optical absorption (MHP/ternary BHJ (FAPbI ₃ / $\text{PM}_6\text{BTBP-eC9:BTBP-2F2Cl-P2TH}$))	ITO/SnO _x /MHP/PM ₆ :BTBP-eC9:BTBP-2F2Cl-P2TH/C ₆₀ /BCP/Ag	3.74 nA cm ⁻² (−0.2 V)	$>10^{13}$ (800–900 nm)	9.02/11.42 μs	—	179
^a Noise signal: the noise signal in photodetection is recorded by utilizing a fast Fourier transform signal analyzer combined with a preamplifier to capture the noise current at various frequencies. ^b TPC extracted: speed here can be defined as the time at which the photocurrent decays from the peak to the original 1/e extracted from the transient photocurrent curves. ^c Detection limit: the detection limit in X-ray detection is defined as the equivalent dose rate to produce a photocurrent greater than three times the noise current (dark current). ^d Drifting: drifting means the dark current drift period D .						

^a Noise signal: the noise signal in photodetection is recorded by utilizing a fast Fourier transform signal analyzer combined with a preamplifier to capture the noise current at various frequencies. ^b TPC extracted: speed here can be defined as the time at which the photocurrent decays from the peak to the original 1/e extracted from the transient photocurrent curves. ^c Detection limit: the detection limit in X-ray detection is defined as the equivalent dose rate to produce a photocurrent greater than three times the noise current (dark current). ^d Drifting: drifting means the dark current drift period D .

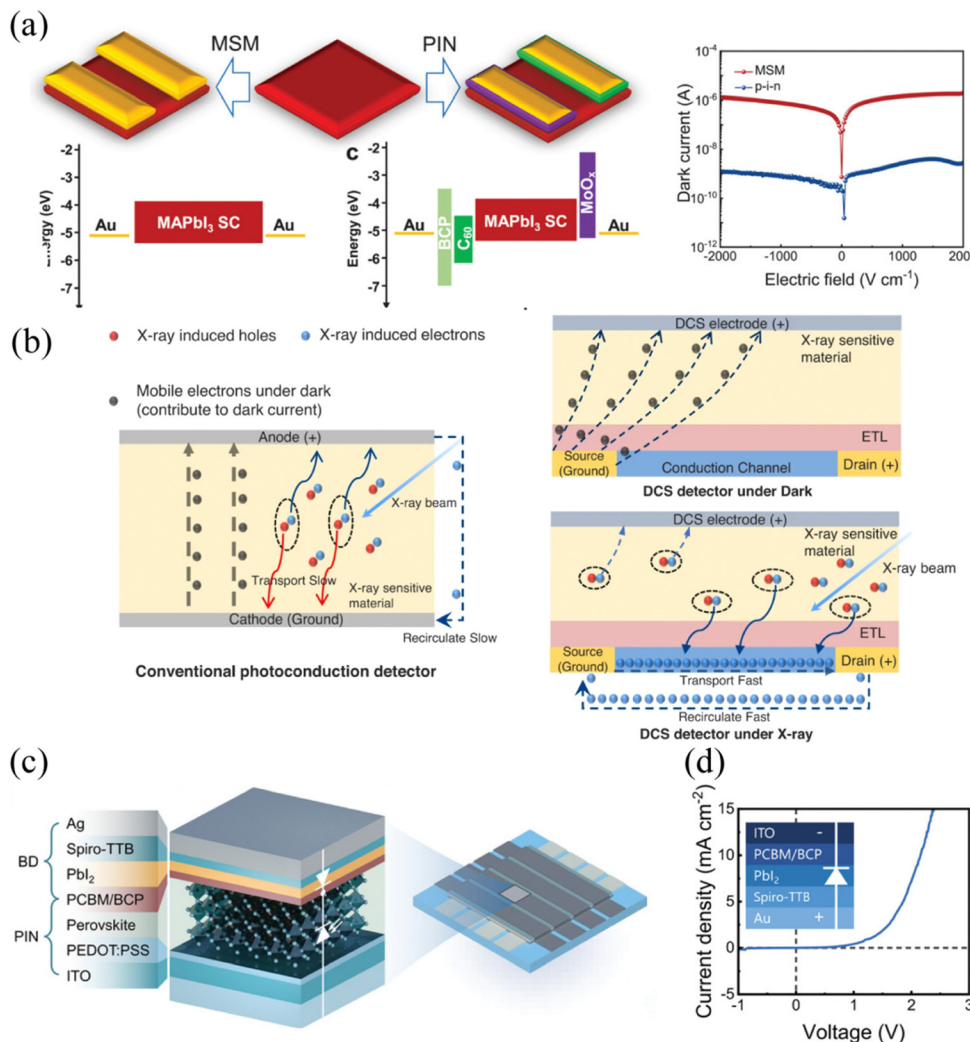


Fig. 13 (a) The schematic diagram, the energy level diagram, and dark current curves of the metal–semiconductor–metal (MSM) and lateral P–I–N devices. Reproduced with permission.¹⁸⁰ Copyright 2021, Wiley–VCH. (b) The schematic illustration of the conventional and dark-current-shunting MHPPD under dark and X-ray radiation. Reproduced with permission.¹⁸¹ Copyright 2023, Nature. (c) The structure of an integrated PIN-blocking diode. (d) Current–voltage (I – V) curves of the blocking diode. Reproduced with permission.¹⁸² Copyright 2022, Wiley–VCH.

temperature range to strike a balance between suppressing J_d while sustaining overall device effectiveness.

Additionally, thorough testing and accurate characterization of MHPPDs are imperative.¹⁸⁹ Common issues include the overestimation of D^* due to the oversight of noise currents other than J_d ,¹⁹⁰ the challenges in testing MHPPDs for direct X-ray detection under atmospheric conditions,¹⁹¹ and incorrect application of formulas or linear fitting in assessing the LDR of MHPPDs.¹⁹² Implementing advanced characterization techniques is fundamental to elucidate the chemical, morphological, structural, and optoelectronic attributes of MHPs, which assist in mitigating J_d in MHPPDs. Techniques such as UV-visible-NIR spectroscopy, photoluminescence (PL), time-resolved PL, and transient absorption spectroscopy are instrumental in directly assessing the light absorption and luminescence properties of MHPs. Electron microscopies like scanning electron microscopy (SEM), transmission electron microscopy (TEM), atomic

force microscopy (AFM) combined with conductive AFM (c-AFM), and energy-dispersive X-ray (EDX) spectroscopy provide in-depth analysis of chemical, morphological, and structural properties at the interface of MHPs. Depth-profiling techniques, including X-ray photoelectron spectroscopy (XPS) and time-of-flight secondary ion mass spectrometry (TOF-SIMS), are crucial for profiling the chemical composition through the depth of MHPs. Characterization techniques geared towards electrical properties, such as electrochemical impedance spectroscopy (EIS), space-charge-limited currents, and transient photovoltage/photocurrent studies, are critical for investigating charge transport and extraction dynamics in MHPPDs. By leveraging these advanced techniques and refining the associated methodologies, we can better differentiate the performance attributes of MHPs, address their intrinsic challenges, and drive forward the performance of MHPPDs. In conclusion, as research continues to focus on suppressing J_d

Strategy	Device structure	Dark current (density) (I_d or D^* (Jones))	Speed [rise time (t_r)/ fall (decay) time (t_f)] (dB)	LDR Ref.
Regulate band alignment and promote band bending (MAPbI ₃ integrated Au/MHP/BPMoS ₂ with a 2D photogate photodiode)	ITO/PEDOT:PSS/MHP/PCBM/BCP/ Pbl ₂ /Spiro-TPB/Ag	3 × 10 ⁻¹¹ A	1.3 × 10 ¹²	150/240 μs
Regulate band alignment and promote band bending (PIN PPDs stacked by a reverse blocking diode and the PCB/MHP as the co-cathode)	Ag/MAPbI ₃ /Au	—	2.1 × 10 ¹² (710 nm)	61.2/72.8 ns
Regulate band alignment and promote band bending (asymmetric contact electrodes Ag/MAPbI ₃ /Au)	ITO/TaTm:F ₆ -TCNNQ/MHP/TaTm:F ₆ - (MHP-based photodiode integrated with MHP-based photoconductor)	3.6 × 10 ⁻¹⁶ A Hz ^{-1/2} (noise signal) ^a	1.3 × 10 ¹² (520 nm)	—
Establish the built-in electrical field and manage the optical absorption (lateral device BCP/C ₆₀ /MAPbI ₃ /MoO ₃ /Au MAPbI ₃ /MoO ₃)	TCNNQ/TaTm/MHP/C ₆₀ /BCP/Ag	1.1 × 10 ⁻⁴ mA cm ⁻² (−1 V, about 8 times reduced)	1.7 × 10 ¹² (730 nm)	25.3 μs (TPC extracted) ^b
Eliminate the interfacial electrochemical reaction (lateral device BCP/C ₆₀ /Lateral Au/BCP/C ₆₀ /MAPbI ₃ /MoO ₃ /Au PMMA/Au worked as the top electrode)	265 pA Hz ^{-1/2} (noise signal) ^a	0.1 nGy s ⁻¹ (about 10 ³ times reduced)	420/470 μs	63
Impede shunt dark current by employing a top electrode (P-I-N diode integrated a dark-current-shunting electrode)	Au (source)/C ₆₀ /MHP/Au (drain) and PMMA/Au worked as the top electrode	51.1 fA (5 V mm ⁻¹)	7.84 nGy s ⁻¹ (detection limit) ^c	—

^a Noise signal: the noise signal in photodetection is recorded by utilizing a fast Fourier transform signal analyzer combined with a preamplifier to capture the noise current at various frequencies. ^b TPC extracted: speed here can be defined as the time at which the photocurrent decays from the peak to the original 1/e extracted from the transient photocurrent curves. ^c Detection limit: the detection limit in X-ray detection is defined as the equivalent dose rate to produce a photocurrent greater than three times the noise current (dark current).

and improving the reliability and functionality of MHPPDs, their practical application in the field of optoelectronics is becoming increasingly feasible.

Author contributions

Yue Wang, D. Li, and Q. Song conducted the literature review and drafted the manuscript. Yue Wang, D. Li, Yang Wang, Y. Chen contributed to manuscript editing and grammar check. Yue Wang, D. Li, Q. Song, Y. Liu, Yang Wang and Y. Chen secured funding, resources, supervision, and contributed to manuscript editing.

Data availability

No primary research results, software or codes have been included and no new data were generated or analysed as part of this review.

Conflicts of interest

There are no conflicts to declare.

Acknowledgements

This work was supported by the Natural Science Foundation of China (Grant No. 62205062), the Natural Science Foundation of Fujian Province of China (Grant No. 2022J05047, 2023J01087, 2023J01527, 2023J01530), and the Fujian Normal University “Young Talent” Start-up Grant (Grant No. Y0720308K13).

References

- 1 Z. Li, T. Yan and X. Fang, *Nat. Rev. Mater.*, 2023, **8**, 587–603.
- 2 F. Cao, L. Liu and L. Li, *Mater. Today*, 2023, **62**, 327–349.
- 3 S. Mauthe, Y. Baumgartner, M. Sousa, Q. Ding, M. D. Rossell, A. Schenk, L. Czornomaz and K. E. Moselund, *Nat. Commun.*, 2020, **11**, 4565.
- 4 R. Tian, X. Gan, C. Li, X. Chen, S. Hu, L. Gu, D. Van Thourhout, A. Castellanos-Gomez, Z. Sun and J. Zhao, *Light: Sci. Appl.*, 2022, **11**, 101.
- 5 F. P. García De Arquer, A. Armin, P. Meredith and E. H. Sargent, *Nat. Rev. Mater.*, 2017, **2**, 16100.
- 6 Q. Qiu and Z. Huang, *Adv. Mater.*, 2021, **33**, 2008126.
- 7 W. Ouyang, J. Chen, Z. Shi and X. Fang, *Appl. Phys. Rev.*, 2021, **8**, 31315.
- 8 G. Long, R. Sabatini, M. I. Saidaminov, G. Lakhwani, A. Rasmita, X. Liu, E. H. Sargent and W. Gao, *Nat. Rev. Mater.*, 2020, **5**, 423–439.
- 9 Q. Lin, A. Armin, P. L. Burn and P. Meredith, *Nat. Photonics*, 2015, **9**, 687–694.
- 10 Y. Fang and J. Huang, *Adv. Mater.*, 2015, **27**, 2804–2810.
- 11 C. Li, H. Wang, F. Wang, T. Li, M. Xu, H. Wang, Z. Wang, X. Zhan, W. Hu and L. Shen, *Light: Sci. Appl.*, 2020, **9**, 31.

12 C. Chen, Z. Wang, J. Wu, Z. Deng, T. Zhang, Z. Zhu, Y. Jin, B. Lew, I. Srivastava, Z. Liang, S. Nie and V. Gruev, *Sci. Adv.*, 2023, **9**, eadk3860.

13 S. Tie, S. Dong, R. Yuan, B. Cai, J. Zhu and X. Zheng, *Chem. Commun.*, 2023, **59**, 5016–5029.

14 P. Kumar, V. K. Shukla, M. Kim and R. Singh, *Sens. Actuators, A*, 2024, **369**, 115076.

15 Z. Xiao, Z. Song and Y. Yan, *Adv. Mater.*, 2019, **31**, 1803792.

16 G. Kakavelakis, M. Gedda, A. Panagiotopoulos, E. Kymakis, T. D. Anthopoulos and K. Petridis, *Adv. Sci.*, 2020, **7**, 2002098.

17 Q. A. Akkerman, V. D. Innocenzo, S. Accornero, A. Scarpellini, A. Petrozza, M. Prato and L. Manna, *J. Am. Chem. Soc.*, 2015, **137**, 10276–10281.

18 X. Li, J. M. Hoffman and M. G. Kanatzidis, *Chem. Rev.*, 2021, **121**, 2230–2291.

19 C. Zhou, H. Lin, Q. He, L. Xu, M. Worku, M. Chaaban, S. Lee, X. Shi, M. Du and B. Ma, *Mater. Sci. Eng., R*, 2019, **137**, 38–65.

20 A. Dey, J. Ye, A. De, E. Debroye, S. K. Ha, E. Bladt, A. S. Kshirsagar, Z. Wang, J. Yin, Y. Wang, L. N. Quan, F. Yan, M. Gao, X. Li, J. Shamsi, T. Debnath, M. Cao, M. A. Scheel, S. Kumar, J. A. Steele, M. Gerhard, L. Chouhan, K. Xu, X. Wu, Y. Li, Y. Zhang, A. Dutta, C. Han, I. Vincon, A. L. Rogach, A. Nag, A. Samanta, B. A. Korgel, C. Shih, D. R. Gamelin, D. H. Son, H. Zeng, H. Zhong, H. Sun, H. V. Demir, I. G. Scheblykin, I. Mora-Seró, J. K. Stolarczyk, J. Z. Zhang, J. Feldmann, J. Hofkens, J. M. Luther, J. Pérez-Prieto, L. Li, L. Manna, M. I. Bodnarchuk, M. V. Kovalenko, M. B. J. Roeffaers, N. Pradhan, O. F. Mohammed, O. M. Bakr, P. Yang, P. Müller-Buschbaum, P. V. Kamat, Q. Bao, Q. Zhang, R. Krahne, R. E. Galian, S. D. Stranks, S. Bals, V. Biju, W. A. Tisdale, Y. Yan, R. L. Z. Hoye, L. Polavarapu and G. C. U. S. National Renewable Energy Lab. Nrel and O. V. S. Univ., *ACS Nano*, 2021, **15**, 10775–10981.

21 J. S. Manser, J. A. Christians and P. V. Kamat, *Chem. Rev.*, 2016, **116**, 12956–13008.

22 C. Neusel, H. Jelitto and G. A. Schneider, *J. Appl. Phys.*, 2015, **117**, 154902.

23 J. Chen and N. G. Park, *Adv. Mater.*, 2019, **31**, 1803019.

24 W. Jang, K. Kim, B. G. Kim, J. S. Nam, I. Jeon and D. H. Wang, *Adv. Funct. Mater.*, 2022, **32**, 2207713.

25 J. Yang, H. Zhang, H. Cui, S. Xu, G. Pan, H. Gao, Z. Zhang and Y. Mao, *ACS Photonics*, 2024, **11**, 1181–1188.

26 V. M. Le Corre, M. B. Johnston, L. J. A. Koster, J. Lim and H. J. Snaith, *Energy Environ. Sci.*, 2021, **15**(17), 14006–14760.

27 Z. Y. Yin, Y. Chen, Y. Y. Zhang, Y. Yuan, Q. Yang, Y. N. Zhong, X. Gao, J. Xiao, Z. K. Wang, J. L. Xu and S. D. Wang, *Adv. Funct. Mater.*, 2023, **33**, 2302199.

28 O. D. I. Moseley, B. Roose, S. J. Zelewski and S. D. Stranks, *ACS Appl. Energy Mater.*, 2023, **6**, 10233–10242.

29 R. Ollearo, J. Wang, M. J. Dyson, C. H. L. Weijtens, M. Fattori, B. T. van Gorkom, A. J. J. M. van Breemen, S. C. J. Meskers, R. A. J. Janssen and G. H. Gelinck, *Nat. Commun.*, 2021, **12**, 7277.

30 O. Almora, D. Miravet, I. Gelmetti and G. Garcia-Belmonte, *Phys. Status Solidi RRL*, 2022, **16**, 2200336.

31 B. R. Sutherland, A. K. Johnston, A. H. Ip, J. Xu, V. Adinolfi, P. Kanjanaboops and E. H. Sargent, *ACS Photonics*, 2015, **2**, 1117–1123.

32 E. A. Duijnste, V. M. Le Corre, M. B. Johnston, L. J. A. Koster, J. Lim and H. J. Snaith, *Phys. Rev. Appl.*, 2021, **15**, 014006.

33 A. Datta, J. Fiala, P. Becla and S. Motakef, *APL Mater.*, 2017, **5**, 106109.

34 K. T. Ho, S. F. Leung, T. Y. Li, P. Maity, B. Cheng, H. C. Fu, O. F. Mohammed and J. H. He, *Adv. Mater.*, 2018, **30**, 1804372.

35 T. S. Ripples, A. K. Baranwal, K. Nishinaka, Y. Ogomi, G. Garcia-Belmonte and S. Hayase, *Phys. Chem. Chem. Phys.*, 2016, **18**, 14970–14975.

36 Y. Shao, Y. Fang, T. Li, Q. Wang, Q. Dong, Y. Deng, Y. Yuan, H. Wei, M. Wang, A. Gruverman, J. Shield, J. Huang and L. N. U. S. Univ. Of Nebraska, *Energy Environ. Sci.*, 2016, **9**, 1752–1759.

37 S. E. J. O’Kane, G. Richardson, A. Pockett, R. G. Niemann, J. M. Cave, N. Sakai, G. E. Eperon, H. J. Snaith, J. M. Foster, P. J. Cameron and A. B. Walker, *J. Mater. Chem. C*, 2017, **5**, 452–462.

38 T. Y. Yang, G. Gregori, N. Pellet, M. Gratzel and J. Maier, *Angew. Chem., Int. Ed.*, 2015, **54**, 7905–7910.

39 M. García-Batlle, S. Deumel, J. E. Huerdler, S. F. Tedde, O. Almora and G. Garcia-Belmonte, *Adv. Photonics Res.*, 2022, **3**, 2200136.

40 Y. Yun, G. S. Han, G. N. Park, J. Kim, J. Park, D. Vidyasagar, J. Jung, W. C. Choi, Y. J. Choi, K. Heo, J. Kang, J. S. Park, H. S. Jung and S. Lee, *Adv. Mater.*, 2022, **34**, 2206932.

41 Y. Liu, Y. Zhang, X. Zhu, J. Feng, I. Spanopoulos, W. Ke, Y. He, X. Ren, Z. Yang, F. Xiao, K. Zhao, M. Kanatzidis and S. F. Liu, *Adv. Mater.*, 2021, **33**, 2006010.

42 F. Furlan, D. Nodari, E. Palladino, E. Angela, L. Mohan, J. Briscoe, M. J. Fuchter, T. J. Macdonald, G. Grancini, M. A. McLachlan and N. Gasparini, *Adv. Opt. Mater.*, 2022, **10**, 2201816.

43 L. Li, F. Zhang, S. Ye, X. Peng, Z. Sun, J. Lian, L. Liu, J. Qu and J. Song, *Nano Energy*, 2020, **71**, 104611.

44 Y. Wang, D. Yang, D. Ma, D. H. Kim, T. Ahamad, S. M. Alshehri and A. Vadim, *Sci. China: Mater.*, 2019, **62**, 790–796.

45 D. Liu, B. Yu, M. Liao, Z. Jin, L. Zhou, X. Zhang, F. Wang, H. He, T. Gatti and Z. He, *ACS Appl. Mater. Interfaces*, 2020, **12**, 30530–30537.

46 F. Yao, P. Gui, C. Chen, B. Li, R. Li, C. Tao, Q. Lin and G. Fang, *ACS Appl. Mater. Interfaces*, 2019, **11**, 39875–39881.

47 E. Hong, D. Nodari, F. Furlan, E. Angela, J. Panidi, M. A. McLachlan and N. Gasparini, *Adv. Opt. Mater.*, 2024, **12**, 2302712.

48 N. R. Al Amin, C. Lee, Y. Huang, C. Shih, R. Estrada, S. Biring, M. Kuo, C. Li, Y. Huang and S. Liu, *ACS Appl. Mater. Interfaces*, 2023, **15**, 21284–21295.

49 Y. Yun, H. Cho, J. Jung, S. W. Yang, D. Vidyasagar, R. K. Gunasekaran and S. Lee, *J. Mater. Sci. Technol.*, 2023, **152**, 100–108.

50 J. Wu, L. Wang, A. Feng, S. Yang, N. Li, X. Jiang, N. Liu, S. Xie, X. Guo, Y. Fang, Z. Chen, D. Yang and X. Tao, *Adv. Funct. Mater.*, 2022, **32**, 2109149.

51 P. Gui, J. Li, X. Zheng, H. Wang, F. Yao, X. Hu, Y. Liu and G. Fang, *J. Mater. Chem. C*, 2020, **8**, 684–6812.

52 W. Wang, D. Zhao, F. Zhang, L. Li, M. Du, C. Wang, Y. Yu, Q. Huang, M. Zhang, L. Li, J. Miao, Z. Lou, G. Shen, Y. Fang and Y. Yan, *Adv. Funct. Mater.*, 2017, **27**, 1703953.

53 D. Luo, T. Zou, W. Yang, B. Xiang, X. Yang, Y. Wang, R. Su, L. Zhao, R. Zhu, H. Zhou, T. P. Russell, H. Yu and Z. H. Lu, *Adv. Funct. Mater.*, 2020, **30**, 2001692.

54 Y. Zhao, C. Li, J. Jiang, B. Wang and L. Shen, *Small*, 2020, **16**, 2001534.

55 S. Wang, M. Li, C. Song, C. Zheng, J. Li, Z. Li, Y. Zhang and J. Yao, *Appl. Surf. Sci.*, 2023, **623**, 156983.

56 Y. Miao, J. Wu, X. Qi, L. Yang, X. Wang, F. Zheng, F. Zhao, S. Shafique, Y. Zhu and Z. Hu, *Nano Energy*, 2023, **113**, 108605.

57 J. Peng, Y. Xu, F. Yao, H. Huang, R. Li and Q. Lin, *Matter*, 2022, **5**, 2251–2264.

58 L. Guo, Y. Qi, Z. Wu, X. Yang, G. Yan, R. Cong, L. Zhao, W. Zhang, S. Wang, C. Pan and Z. Yang, *Adv. Mater.*, 2023, **35**, 2301705.

59 D. S. Lee, J. H. Heo, J. K. Park, B. W. Kim, H. J. Lee, Y. M. Song and S. H. Im, *ACS Appl. Mater. Interfaces*, 2021, **13**, 16775–16783.

60 F. Zhu, G. Lian, B. Yu, T. Zhang, L. Zhang, H. Yu, D. Cui, Q. Wang, H. Zhang, Q. Meng and C. Wong, *ACS Appl. Mater. Interfaces*, 2022, **14**, 1526–1536.

61 R. Ollearo, A. Caiazzo, J. Li, M. Fattori, A. J. J. M. van Breemen, M. M. Wienk, G. H. Gelinck and R. A. J. Janssen, *Adv. Mater.*, 2022, **34**, 2205261.

62 J. W. Lim, H. Wang, C. H. Choi, H. Kwon, L. N. Quan, W. Park, Y. Noh and D. H. Kim, *Nano Energy*, 2019, **57**, 761–770.

63 H. Tsai, S. Shrestha, L. Pan, H. H. Huang, J. Strzalka, D. Williams, L. Wang, L. R. Cao and W. Nie, *Adv. Mater.*, 2022, **34**, 2106498.

64 R. Li, Y. Xu, W. Li, Y. Li, J. Peng, M. Xu and Q. Lin, *J. Phys. Chem. Lett.*, 2021, **12**, 1726–1733.

65 X. He, M. Xia, H. Wu, X. Du, Z. Song, S. Zhao, X. Chen, G. Niu and J. Tang, *Adv. Funct. Mater.*, 2022, **32**, 2109458.

66 Z. Liao, L. Qiu, T. Chen, W. Qian, Y. Wang, S. Yang, T. Sun, G. Yang, A. K. Srivastava and H. Zhou, *Adv. Mater. Technol.*, 2023, **8**, 2300714.

67 L. Min, W. Tian, F. Cao, J. Guo and L. Li, *Adv. Mater.*, 2021, **33**, 2101714.

68 B. Jiang, G. Yan, Y. Xiao, Y. Yuan, C. Zhao, W. Mai and R. Hong, *J. Mater. Sci.*, 2023, **58**, 7076–7091.

69 Y. Hsiao, J. Song, H. Wu, K. Hong, C. Leu and C. Shih, *J. Alloys Compd.*, 2021, **889**, 161621.

70 X. Zhao, Y. Wang, L. Li, L. Huang, G. Li and W. H. Sun, *J. Mater. Sci.*, 2021, **56**, 9242–9253.

71 Z. Yang, M. Wang, J. Li, J. Dou, H. Qiu and J. Shao, *ACS Appl. Mater. Interfaces*, 2018, **10**, 26387–26395.

72 H. L. Zhu, H. Lin, Z. Song, Z. Wang, F. Ye, H. Zhang, W. Yin, Y. Yan and W. C. H. Choy, *ACS Nano*, 2019, **13**, 11800–11808.

73 W. Li, Y. Xu, J. Peng, R. Li, J. Song, H. Huang, L. Cui and Q. Lin, *ACS Appl. Mater. Interfaces*, 2021, **13**, 2971–2978.

74 C. Bao, Z. Chen, Y. Fang, H. Wei, Y. Deng, X. Xiao, L. Li and J. Huang, *Adv. Mater.*, 2017, **29**, 1703209.

75 V. O. Eze, G. R. Adams, L. Braga Carani, R. J. Simpson and O. I. Okoli, *J. Phys. Chem. C*, 2020, **124**, 20643–20653.

76 M. Sulaman, S. Y. Yang, Z. H. Zhang, A. Imran, A. Bukhtiar, Z. H. Ge, Y. Tang, Y. R. Jiang, L. B. Tang and B. S. Zou, *Mater. Today Phys.*, 2022, **27**, 100829.

77 Y. Zhao, S. Jiao, S. Liu, Y. Jin, S. Yang, X. Wang, T. Liu, H. Jin, D. Wang, S. Gao and J. Wang, *J. Alloys Compd.*, 2023, **965**, 171434.

78 R. Xing, Z. Li, W. Zhao, D. Wang, R. Xie, Y. Chen, L. Wu and X. Fang, *Adv. Mater.*, 2024, **36**, 2310248.

79 Z. Shuang, H. Zhou, D. Wu, X. Zhang, B. Xiao, G. Ma, J. Zhang and H. Wang, *Chem. Eng. J.*, 2022, **433**, 134544.

80 A. A. Khan, N. Kumar, U. Jung, W. Heo, Z. Tan and J. Park, *Nanoscale Horiz.*, 2023, **8**, 1577–1587.

81 Y. Yan, Q. Wu, Y. Zhao, S. Chen, S. Hu, J. Zhu, J. Huang and Z. Liang, *Small*, 2018, **14**, 1802764.

82 H. Di, W. Zeng, B. H. Li, F. Liao, C. Zhao, C. Liang, H. Li, J. C. Wang, D. B. Cheng, Z. Ren and Y. Zhao, *Adv. Sci.*, 2023, **10**, 2302917.

83 L. He, G. Hu, J. Jiang, W. Wei, X. Xue, K. Fan, H. Huang and L. Shen, *Adv. Mater.*, 2023, **35**, 2210016.

84 Z. Gao, Y. Zheng, G. Huang, G. Yang, X. Yu and J. Yu, *Micromachines*, 2020, **11**, 1090.

85 D. Zhang, H. Wei and L. Zhu, *Org. Electron.*, 2023, **114**, 106726.

86 M. Xia, Z. Song, H. Wu, X. Du, X. He, J. Pang, H. Luo, L. Jin, G. Li, G. Niu and J. Tang, *Adv. Funct. Mater.*, 2022, **32**, 2110729.

87 H. Zhou, R. Wang, X. Zhang, B. Xiao, Z. Shuang, D. Wu and P. Qin, *Chem. Commun.*, 2023, **59**, 8544–8547.

88 L. Jiang, Z. Li, Q. Dong, X. Rong and G. Dong, *ACS Appl. Mater. Interfaces*, 2023, **15**, 32647–32655.

89 X. Xu, C. C. Chueh, P. Jing, Z. Yang, X. Shi, T. Zhao, L. Y. Lin and A. K. Y. Jen, *Adv. Funct. Mater.*, 2017, **27**, 1701053.

90 S. Wang, T. Li, Q. Li, H. Zhao, C. Zheng, M. Li, J. Li, Y. Zhang and J. Yao, *J. Mater. Chem. C*, 2022, **10**, 7886–7895.

91 F. Liu, K. Liu, S. Rafique, Z. Xu, W. Niu, X. Li, Y. Wang, L. Deng, J. Wang, X. Yue, T. Li, J. Wang, P. Ayala, C. Cong, Y. Qin, A. Yu, N. Chi and Y. Zhan, *Adv. Sci.*, 2023, **10**, 2205879.

92 J. H. Lu, M. T. Cheng, H. L. Hsu, S. W. Liu and C. P. Chen, *Adv. Funct. Mater.*, 2020, **30**, 2002503.

93 R. Li, J. Peng, Y. Xu, W. Li, L. Cui, Y. Li and Q. Lin, *Adv. Opt. Mater.*, 2021, **9**, 2001587.

94 Y. Wang, S. Ye, Z. Sun, J. Zhu, Y. Liu, R. Wang, F. Lin, W. Zhang, Y. Yang and C. Wang, *ACS Appl. Mater. Interfaces*, 2023, **15**, 59005–59015.

95 Z. Gao, H. Zhou, K. Dong, C. Wang, J. Wei, Z. Li, J. Li, Y. Liu, J. Zhao and G. Fang, *Nano-Micro Lett.*, 2022, **14**, 215.

96 Z. Jia, J. Peng, L. Yu, T. Jiang, Y. Li, F. Yao, F. Ren and Q. Lin, *Chem. Eng. J.*, 2022, **450**, 138229.

97 H. Zhao, T. Li, J. Li, Q. Li, S. Wang, C. Zheng, J. Li, M. Li, Y. Zhang and J. Yao, *J. Alloys Compd.*, 2022, **908**, 164482.

98 J. Li, J. Ran, Z. Uddin, J. Li, F. Wan, Y. Yuan, J. Chen and B. Yang, *ACS Appl. Energy Mater.*, 2022, **5**, 12158–12164.

99 B. Jo, K. M. Kim, S. Lee, H. J. Kim, J. Kim, J. Kang, G. Namkoong, G. S. Han and H. S. Jung, *Chem. Mater.*, 2023, **35**, 10495–10503.

100 H. Liu, L. Zhu, H. Zhang, X. He, F. Yan, K. S. Wong and W. C. H. Choy, *ACS Energy Lett.*, 2023, **8**, 577–589.

101 W. Kim, J. Park, Y. Aggarwal, S. Sharma, E. H. Choi and B. Park, *Nanomaterials*, 2023, **13**, 619.

102 N. Ma, J. Jiang, Y. Zhao, L. He, Y. Ma, H. Wang, L. Zhang, C. Shan, L. Shen and W. Hu, *Nano Energy*, 2021, **86**, 106113.

103 Y. Aggarwal, J. Park, W. Kim, S. Sharma, H. Jeong, M. G. Kim, J. Kil, E. H. Choi and B. Park, *Sol. Energy Mater. Sol. Cells*, 2024, **270**, 112815.

104 M. Wang, H. Sun, F. Cao, W. Tian and L. Li, *Adv. Mater.*, 2021, **33**, 2100625.

105 Q. Lin, A. Armin, D. M. Lyons, P. L. Burn and P. Meredith, *Adv. Mater.*, 2015, **27**, 2060–2064.

106 C. Bao, J. Yang, S. Bai, W. Xu, Z. Yan, Q. Xu, J. Liu, W. Zhang and F. Gao, *Adv. Mater.*, 2018, **30**, 1803422.

107 G. Cen, Y. Liu, C. Zhao, G. Wang, Y. Fu, G. Yan, Y. Yuan, C. Su, Z. Zhao and W. Mai, *Small*, 2019, **15**, 1902135.

108 S. Demchyshyn, M. Verdi, L. Basiricò, A. Ciavatti, B. Hailegnaw, D. Cavalcoli, M. C. Scharber, N. S. Sariciftci, M. Kaltenbrunner and B. Fraboni, *Adv. Sci.*, 2020, **7**, 2002586.

109 X. Zhang, Z. Li, T. Yan, L. Su and X. Fang, *Small*, 2023, **19**, 2206310.

110 J. Y. Chun, B. G. Kim, J. Y. Kim, W. Jang and D. H. Wang, *Carbon Energy*, 2023, **5**, e350.

111 C. Li, J. Lu, Y. Zhao, L. Sun, G. Wang, Y. Ma, S. Zhang, J. Zhou, L. Shen and W. Huang, *Small*, 2019, **15**, 1903599.

112 W. Wei, Y. Zhang, Q. Xu, H. Wei, Y. Fang, Q. Wang, Y. Deng, T. Li, A. Gruverman, L. Cao and J. Huang, *Nat. Photonics*, 2017, **11**, 315–321.

113 H. L. Zhu, J. Cheng, D. Zhang, C. Liang, C. J. Reckmeier, H. Huang, A. L. Rogach and W. C. H. Choy, *ACS Nano*, 2016, **10**, 6808–6815.

114 B. Pan, M. Wu, G. Yang, D. Zhao and J. Yu, *Opt. Lett.*, 2020, **45**, 5860–5863.

115 Z. Liu, Z. Zhang, X. Zhang, X. Li, Z. Liu, G. Liao, Y. Shen and M. Wang, *Nano Lett.*, 2023, **23**, 1181–1188.

116 Z. Chen, H. Wang, F. Li, W. Zhang, Y. Shao and S. Yang, *ACS Appl. Mater. Interfaces*, 2023, **15**, 51370–51379.

117 L. He, M. Li, Q. Chen, R. Sun, F. Wang, X. Wang, H. Wu, W. Wei, T. Qin and L. Shen, *ACS Appl. Mater. Interfaces*, 2022, **14**, 46809–46818.

118 G. Li, Y. Wang, L. Huang and W. Sun, *J. Alloys Compd.*, 2022, **907**, 164432.

119 M. Sulaman, Y. Song, S. Yang, M. I. Saleem, M. Li, C. Perumal Veeramalai, R. Zhi, Y. Jiang, Y. Cui, Q. Hao and B. Zou, *ACS Appl. Mater. Interfaces*, 2020, **12**, 26153–26160.

120 D. H. Shin, S. H. Shin and S. Choi, *Appl. Surf. Sci.*, 2020, **514**, 145880.

121 L. He, D. Wang, Y. Zhao, Y. Zhang, W. Wei and L. Shen, *J. Mater. Chem. C*, 2021, **9**, 11722–11728.

122 C. Shan, F. Meng, J. Yu, Z. Wang, W. Li, D. Fan, R. Chen, H. Ma, G. Li and A. K. K. Kyaw, *J. Mater. Chem. C*, 2021, **9**, 7632–7642.

123 J. Yang, Y. Wang, L. Huang, G. Li, X. Qiu, X. Zhang and W. Sun, *J. Phys. Chem. Lett.*, 2022, **13**, 3904–3914.

124 J. Park, Y. Aggarwal, W. Kim, S. Sharma, E. H. Choi and B. Park, *Opt. Express*, 2023, **31**, 1202.

125 L. Dou, Y. Yang, J. You, Z. Hong, W. Chang, G. Li and Y. Yang, *Nat. Commun.*, 2014, **5**, 5404.

126 L. Huang, Y. Wang, X. Zhu, X. Zhao, G. Li, L. Li and W. Sun, *J. Phys. Chem. C*, 2021, **125**, 16066–16074.

127 R. Guo, F. Huang, K. Zheng, T. Pullerits and J. Tian, *ACS Appl. Mater. Interfaces*, 2018, **10**, 35656–35663.

128 A. M. Afzal, I. G. Bae, Y. Aggarwal, J. Park, H. R. Jeong, E. H. Choi and B. Park, *Sci. Rep.*, 2021, **11**, 169.

129 B. Li, X. Huang, X. Wu, Q. Zuo, Y. Cao, Q. Zhu, Y. Li, Y. Xu, G. Zheng, D. Chen, X. H. Zhu, F. Huang, H. Zhen, L. Hou, J. Qing and W. Cai, *Adv. Funct. Mater.*, 2023, **33**, 2300216.

130 Y. Subramaniam and K. L. Woon, *Synth. Met.*, 2023, **293**, 117261.

131 Y. Liu and Z. Ji, *Appl. Phys. Lett.*, 2023, **122**, 21103.

132 Y. Wang, X. Zhang, Q. Jiang, H. Liu, D. Wang, J. Meng, J. You and Z. Yin, *ACS Appl. Mater. Interfaces*, 2018, **10**, 6505–6512.

133 Y. Yuan, Z. Ji, G. Yan, Z. Li, J. Li, M. Kuang, B. Jiang, L. Zeng, L. Pan and W. Mai, *J. Mater. Sci. Technol.*, 2021, **75**, 39–47.

134 J. Lin, F. Hsu, C. Chang and Y. Chen, *J. Mater. Chem. C*, 2021, **9**, 5190–5197.

135 T. Sun, T. Chen, J. Chen, Q. Lou, Z. Liang, G. Li, X. Lin, G. Yang and H. Zhou, *Nanoscale*, 2023, **15**, 783–7811.

136 F. Tang, Q. Chen, L. Chen, F. Ye, J. Cai and L. Chen, *Appl. Phys. Lett.*, 2016, **109**, 123301.

137 T. Zou, J. Zhang, S. Huang, C. Liu, R. Qiu, X. Wang, W. Wu, H. Wang, Z. Wei, Q. Dai, C. Liu, S. Zhang and H. Zhou, *RSC Adv.*, 2019, **9**, 3800–3808.

138 Z. Ji, G. Cen, C. Su, Y. Liu, Z. Zhao, C. Zhao and W. Mai, *Adv. Opt. Mater.*, 2020, **8**, 2001436.

139 H. Mescher, F. Schackmar, H. Eggers, T. Abzieher, M. Zuber, E. Hamann, T. Baumbach, B. S. Richards, G. Hernandez-Sosa, U. W. Paetzold and U. Lemmer, *ACS Appl. Mater. Interfaces*, 2020, **12**, 15774–15784.

140 C. Liu, K. Wang, C. Yi, X. Shi, P. Du, A. W. Smith, A. Karim and X. Gong, *J. Mater. Chem. C*, 2015, **3**, 66–666.

141 Z. Ji, Y. Liu, W. Li, C. Zhao and W. Mai, *Sci. Bull.*, 2020, **65**, 1371–1379.

142 K. M. Sim, A. Swarnkar, A. Nag and D. S. Chung, *Laser Photonics Rev.*, 2018, **12**, 1700209.

143 T. Ji, H. Zhang, J. Guo, Y. Wang, L. Shi, Y. Wu, W. Wang, G. Li, R. Wen, L. Xiao, Q. Su, B. Xu, H. Chen and Y. Cui, *Adv. Funct. Mater.*, 2023, **33**, 2210548.

144 M. Long, L. Yang, D. An, J. Dai, Y. Wang and X. Yao, *Opt. Mater.*, 2024, **147**, 114652.

145 C. A. R. Perini, A. J. Barker, M. Sala, A. Petrozza and M. Caironi, *Semicond. Sci. Tech.*, 2018, **33**, 94004.

146 B. Bhardwaj, U. Bothra, S. Singh, S. Mills, T. J. Ronningen, S. Krishna and D. Kabra, *Appl. Phys. Rev.*, 2023, **10**, 21419.

147 X. Zhu, Y. Liu, S. Huang, X. Gao, J. Li, H. Sun, P. Wangyang and X. Niu, *ACS Appl. Mater. Interfaces*, 2024, **16**(13), 16474.

148 X. Zhang, D. Chu, B. Jia, Z. Zhao, J. Pi, Z. Yang, Y. Li, J. Hao, R. Shi, X. Dong, Y. Liang, J. Feng, A. Najar, Y. Liu and S. F. Liu, *Adv. Mater.*, 2024, **36**, 2305513.

149 S. Liu, Y. Chen, W. Gao, W. Li, X. Yang, Z. Li, Z. Xiao, Y. Liu and Y. Wang, *Adv. Mater.*, 2023, **35**, 2303544.

150 X. Wang, Y. Xu, Y. Pan, Y. Li, J. Xu, J. Chen, J. Wu, Q. Li, X. Zhang, Z. Zhao, C. Li, E. E. Elemike, D. C. Onwudiwe, J. Akram and W. Lei, *Nano Energy*, 2021, **89**, 106311.

151 C. Zou, D. Yu, M. Lin, B. Shen, Y. Peng, Y. Zheng, H. G. Yang, Y. Hou and S. Yang, *Adv. Funct. Mater.*, 2024, 2316430.

152 Q. Lin, Z. Wang, M. Young, J. B. Patel, R. L. Milot, L. Martinez Maestro, R. R. Lunt, H. J. Snaith, M. B. Johnston and L. M. Herz, *Adv. Funct. Mater.*, 2017, **27**, 1702485.

153 R. Guo, C. Bao, F. Gao and J. Tian, *Adv. Opt. Mater.*, 2020, **8**, 2000557.

154 S. Liu, S. Jiao, H. Lu, Y. Nie, S. Gao, D. Wang, J. Wang and L. Zhao, *J. Alloys Compd.*, 2022, **890**, 161827.

155 D. Shao, W. Zhu, G. Xin, X. Liu, T. Wang, S. Shi, J. Lian and S. Sawyer, *J. Mater. Chem. C*, 2020, **8**, 1819–1825.

156 L. Li, Y. Li, J. Li, Y. Fang and D. Yang, *Adv. Opt. Mater.*, 2023, **11**, 2202276.

157 S. Yin, Y. Cheng, Y. Li, W. Liang, T. Li, J. Ma, D. Wu, Z. Shi and X. Li, *J. Mater. Sci.*, 2021, **56**, 13633–13645.

158 J. Zhao, X. Wang, Y. Pan, Y. Xu, Y. Li, J. Chen, J. Wu, Q. Li, Z. Zhao, X. Zhang, J. Akram, B. S. Bae, H. Yang and W. Lei, *Front. Phys.*, 2021, **9**, 712316.

159 Y. Pan, X. Wang, J. Zhao, Y. Xu, Y. Li, Q. Li, X. Zhang, Z. Zhao, Z. Zhu, C. Jing, W. Jun, E. Emeka Elemike, B. S. Bae and W. Lei, *CrystEngComm*, 2021, **23**, 4954–4962.

160 Y. Liu, Y. Gao, J. Zhi, R. Huang, W. Li, X. Huang, G. Yan, Z. Ji and W. Mai, *Nano Res.*, 2022, **15**, 1094–1101.

161 F. Zhao, K. Xu, X. Luo, Y. Liang, Y. Peng and F. Lu, *Adv. Opt. Mater.*, 2018, **6**, 1700509.

162 V. Anilkumar, A. Mahapatra, J. Nawrocki, R. D. Chavan, P. Yadav and D. Prochowicz, *Adv. Opt. Mater.*, 2024, **12**, 2302032.

163 Y. Pan, X. Wang, Y. Xu, Y. Li, E. E. Elemike, A. Shuja, Q. Li, X. Zhang, J. Chen, Z. Zhao and W. Lei, *Front. Chem.*, 2020, **8**, 791.

164 W. Qu, S. Weng, L. Zhang, M. Sun, B. Liu, W. Du and Y. Zhang, *Appl. Phys. Express*, 2020, **13**, 121001.

165 L. Cui, J. Peng, W. Li, Y. Xu, M. Zheng and Q. Lin, *Phys. Status Solidi R*, 2020, **14**, 1900653.

166 T. Zhu, L. Shen, D. Zhang, J. Zheng and X. Gong, *ACS Appl. Mater. Interfaces*, 2022, **14**, 18744–18750.

167 H. Zhou, Z. Song, P. Tao, H. Lei, P. Gui, J. Mei, H. Wang and G. Fang, *RSC Adv.*, 2016, **6**, 625–628.

168 J. Wang, J. Li, S. Lan, C. Fang, H. Shen, Q. Xiong and D. Li, *ACS Nano*, 2019, **13**, 5473–5484.

169 V. Manjunath, P. K. Mishra, R. Dobhal, S. Bimli, P. M. Shirage, S. Sen, P. A. Shaikh and R. S. Devan, *ACS Appl. Electron. Mater.*, 2021, **3**, 4548–4557.

170 Z. Li, Y. Liu, J. He, G. Yan, G. Cen, B. Jiang, C. Zhao, Y. Yuan and W. Mai, *Surf. Interfaces*, 2022, **29**, 101705.

171 L. Shen, Y. Lin, C. Bao, Y. Bai, Y. Deng, M. Wang, T. Li, Y. Lu, A. Gruverman, W. Li and J. Huang, *Mater. Horiz.*, 2017, **4**, 242–248.

172 Z. Qin, D. Song, Z. Xu, B. Qiao, D. Huang and S. Zhao, *Org. Electron.*, 2020, **76**, 105417.

173 F. Cui, P. Zhang, L. Zhang, Y. Hua, X. Sun, X. Li, G. Zhang and X. Tao, *Chem. Mater.*, 2022, **34**, 9601–9612.

174 C. Liu, H. Chen, P. Lin, H. Hu, Q. Meng, L. Xu, P. Wang, X. Wu and C. Cui, *J. Phys.: Condens. Matter.*, 2022, **34**, 405703.

175 W. Li, L. Liu, M. Tan, Y. He, C. Guo, H. Zhang, H. Wei and B. Yang, *Adv. Funct. Mater.*, 2021, **31**, 2107843.

176 Y. Zhou, L. Zhao, Z. Ni, S. Xu, J. Zhao, X. Xiao and J. Huang, *Sci. Adv.*, 2021, **7**, eabg6716.

177 Y. Wang, D. Yang, X. Zhou, D. Ma, A. Vadim, T. Ahamad and S. M. Alshehri, *Adv. Opt. Mater.*, 2017, **5**, 1700213.

178 C. W. Jang, D. H. Shin and S. Choi, *J. Alloys Compd.*, 2023, **948**, 169716.

179 D. Zhao, Y. Wang, X. Sun, X. Wu, B. Li, S. Zhang, D. Gao, B. Liu, S. Gong, Z. Li, C. Zhang, X. Chen, S. Xiao, S. Yang, Z. Li and Z. Zhu, *Small*, 2023, 2309827.

180 Y. Song, L. Li, M. Hao, W. Bi, A. Wang, Y. Kang, H. Li, X. Li, Y. Fang, D. Yang and Q. Dong, *Adv. Mater.*, 2021, **33**, 2103078.

181 P. Jin, Y. Tang, D. Li, Y. Wang, P. Ran, C. Zhou, Y. Yuan, W. Zhu, T. Liu, K. Liang, C. Kuang, X. Liu, B. Zhu and Y. M. Yang, *Nat. Commun.*, 2023, **14**, 626.

182 Z. Zhan, D. Lin, J. Cai, Y. Lu, A. Chen, T. Zhang, K. Chen, P. Liu, X. Wang and W. Xie, *Adv. Mater.*, 2022, **34**, 2207106.

183 L. Wang, X. Zou, J. Lin, J. Jiang, Y. Liu, X. Liu, X. Zhao, Y. F. Liu, J. C. Ho and L. Liao, *ACS Nano*, 2019, **13**, 4804–4813.

184 C. Y. Wu, W. Peng, T. Fang, B. Wang, C. Xie, L. Wang, W. H. Yang and L. B. Luo, *Adv. Electron. Mater.*, 2019, **5**, 1900135.

185 L. Martínez Goyeneche, L. Gil Escrig, I. Susic, D. Tordera, H. J. Bolink and M. Sessolo, *Adv. Opt. Mater.*, 2022, **10**, 2201047.

186 G. Cen, Y. Lv, Y. Yuan, G. Yan, Z. Ji, C. Zhao and W. Mai, *J. Mater. Chem. C*, 2023, **11**, 9341–9347.

187 Y. Zhou, X. Qiu, Z. A. Wan, Z. Long, S. Poddar, Q. Zhang, Y. Ding, C. L. J. Chan, D. Zhang, K. Zhou, Y. Lin and Z. Fan, *Nano Energy*, 2022, **100**, 107516.

188 L. Li, H. Chen, Z. Fang, X. Meng, C. Zuo, M. Lv, Y. Tian, Y. Fang, Z. Xiao, C. Shan, Z. Xiao, Z. Jin, G. Shen, L. Shen and L. Ding, *Adv. Mater.*, 2020, **32**, 1907257.

189 F. Wang, T. Zhang, R. Xie, Z. Wang and W. Hu, *Nat. Commun.*, 2023, **14**, 2224.

190 Y. Fang, A. Armin, P. Meredith and J. Huang, *Nat. Photonics*, 2019, **13**, 1–4.

191 Y. Haruta, P. Huber, A. Hart, M. Bazalova-Carter and M. I. Saidaminov, *ACS Energy Lett.*, 2024, **9**, 271–274.

192 H. T. Chandran, S. Mahadevan, R. Ma, Y. Tang, T. Zhu, F. Zhu, S. Tsang and G. Li, *Appl. Phys. Lett.*, 2024, **124**, 101113.